JM PAPERS

The accelerated propagation of pulsed gravity currents

Damilola Adekanye[1,2] , **Paul Andrew Allen**[1] , **Viet Luan Ho**[3] ,
Gareth M. Keevil[3] , **Martin Schönherr**[4] , **Martin Geier**[4] , **Amirul Khan**[5] ,
William D. McCaffrey[3] **and Robert Michael Dorrell**[6,7]

[1]EPSRC Centre for Doctoral Training in Fluid Dynamics, School of Computing, University of Leeds, Leeds LS2 9JT, UK

[2]First Light Fusion Ltd, Unit 9/10, Oxford Pioneer Park, Mead Road, Yarnton, Kidlington OX5 1QU, UK

[3]School of Earth and Environment, University of Leeds, Leeds LS2 9JT, UK

[4]Institute for Computational Modelling in Civil Engineering, TU Braunschweig, Pockelsstr 3, 38106 Brunswick, Germany

[5]Water, Public Health & Environmental Engineering Group, School of Civil Engineering, University of Leeds, Leeds LS2 9JT, UK

[6]Energy and Environment Institute, University of Hull, Hull HU6 7RX, UK

[7]School of Architecture, Building and Civil Engineering, Loughborough University, Loughborough LE11 3TU, UK

Corresponding author: Damilola Adekanye, damilolaadekanye@gmail.com

Pulsed gravity currents are generated by the sequential release of dense material into a lighter ambient. We investigate the dynamics of pulsed gravity currents using physical scale experiments, two-dimensional depth-averaged shallow water equation (SWE) based models and three-dimensional lattice Boltzmann method (LBM) simulations. Integrating these results we show for the first time that short duration pulsed releases generate intrusive layers, which accelerate front propagation relative to an instantaneously released current of the same total volume. Conversely, a long delay time between pulses produces a current that propagates slower than an equivalent instantaneous release. This finding is supported by physical experiments and depth-resolving LBM simulations. The depth-resolving simulations show that intrusions in pulsed flows experience less drag resistance than those generated by instantaneous releases. The depth-averaged model considered in the present study does not accurately capture the intrusive flow dynamics of pulsed currents. However, the limitations of the finite-depth SWE model may be mitigated by extensions to incorporate entrainment and density stratification. The results also motivate

further research into the impact of buoyancy Reynolds number and channel slope on the propagation of pulsed currents.

Key words: gravity currents, shallow water flows, multiphase flow

---

1. Introduction

Gravity currents are flows driven by natural convection, where gravity acts on a density gradient within a fluid (Huppert 2006; Wells & Dorrell 2021). These buoyancy-driven flows are ubiquitous in both industrial and environmental settings, where gradients in fluid density may arise due to spatial variation in temperature, or in the concentration of suspended particulate or solute material.

Environmental gravity currents are often large-scale events that may cause significant hazards to both human life and structures. Naturally occurring examples include pyroclastic flows, powder-snow avalanches and turbidity currents. Pyroclastic flows, dense surface currents consisting of volcanic material and interstitial air, pose some of the most significant geohazard risks following a volcanic eruption. This is due to the high temperatures and speeds with which they propagate, often over $30 \, \mathrm{m \, s^{-1}}$ and $500 \, ^\circ\mathrm{C}$, with a current thickness typically of the order of hundreds of metres (Wilson 2008). Powder-snow avalanches are a widely known form of gravity current on the Earth's surface. They are driven by the suspension of snow particles, with air forming the interstitial fluid (Hopfinger 1983). Turbidity currents are ocean-floor sedimentary gravity currents that can run-out for thousands of kilometres along the ocean floor. Their deposits can host important natural resources (Reece, Dorrell & Straub 2024). They travel with depth-averaged velocities of 0.1–$6.6 \, \mathrm{m \, s^{-1}}$, a current thickness of 95–$135 \, \mathrm{m}$, and may pose a threat to ocean floor infrastructure such as pipelines and telecommunication cables (Meiburg & Kneller 2010; Peakall & Sumner 2015; Wells & Dorrell 2021).

The current and ambient fluid have initial densities of ρ_0 and ρ_a, respectively. The system has a reduced gravity $g' = g(\rho_0 - \rho_a)/\rho_a$, where g is the acceleration due to gravity. When $(\rho_0 - \rho_a)/\rho_a \ll 1$ the current can be modelled using the Boussinesq approximation, where density variations within the fluid are neglected in the governing equations unless they are acted on by gravity (Meiburg & Kneller 2010; Tritton 2012; Fukuda *et al.* 2023). Non-Boussinesq flows are beyond the scope of the present study.

Environmental gravity currents are challenging to observe directly due to their large scale, infrequent and destructive nature. The dynamics of dilute currents are studied using theoretical, experimental and numerical modelling. Quantifying and predicting front propagation speeds is of particular interest when studying the dynamics of gravity currents. Canonical idealised models consider a 'lock-gate' release of a denser than ambient fluid (Huppert & Simpson 1980; Rottman & Simpson 1983; Hogg 2006; Meiburg, Radhakrishnan & Nasr-Azadani 2015). Such models consist of a straight channel with a gate, separating a relatively dense fluid of concentration ρ_0, from a lighter ambient fluid of concentration $\rho_a < \rho_0$. When the gate is removed a horizontal hydrostatic pressure gradient is created, which induces a gravity current to propagate along the channel (Huppert & Simpson 1980; Andrews & Manga 2012). The characteristic length scale in the vertical and horizontal directions are taken to be the initial current depth h_0, and lock length x_0, respectively. The buoyancy velocity, $U_b = \sqrt{g' h_0}$, is the characteristic velocity scale. The non-dimensional parameters that govern the dynamics of the lock-exchange gravity current are the buoyancy Reynolds number,

$$Re_b = (U_b h_0)/(\nu), \tag{1.1}$$

and Schmidt number,

$$Sc = \nu/D; \tag{1.2}$$

where ν is the kinematic viscosity of the ambient fluid, and D is the diffusivity of the scalar concentration field.

Following a brief acceleration phase, gravity currents transition through three distinct phases: slumping, inertial and viscous (Huppert & Simpson 1980). In the slumping phase the current propagates at a constant velocity referred to as the buoyancy Froude number, $Fr_b = u_f/U_b$, under a balance of pressure and drag forces. The inertial phase is governed by a balance of inertial and buoyancy forces, where front location scales like $x_f \propto t^{(2/3)}$ (Fay 1971; Hoult 1972; Huppert & Simpson 1980; Hogg 2006; Cantero *et al.* 2007). The viscous phase is governed by a balance of viscous and buoyancy forces, where front location scales like $x_f \propto t^{(1/5)}$ (Hoult 1972; Huppert 1982; Cantero *et al.* 2007).

Standard lock-exchange experiments model an environmental flow in which a finite volume of dense fluid is instantaneously released. However, in naturally occurring currents dense material is often released in successive stages, generating pulsed currents. Pulsed flows have various potential causes, including temporal variation in seismic activity, retrogressive slope failure and the confluence of two gravity current flows (Mulder & Alexander 2001; Beeson, Johnson & Goldfinger 2017; Goldfinger *et al.* 2017; Johnson *et al.* 2017). The geological record at the Cascadia margin, Washington, USA, provides evidence of deposits formed by the merging of turbidity currents at multiple channel confluences (Goldfinger *et al.* 2017).

The pyroclastic flow generated by the Soufrière Hills Volcano eruption in 1997 contained three distinct current releases. However, hazard assessments assumed a single release (Loughlin *et al.* 2002). Using the details documented by Loughlin *et al.* (2002) we can estimate the non-dimensional delay time between the first and second pulse. Loughlin *et al.* (2002) states that the current eruption was associated with three seismic events, which occurred at times 12:57:15 ($\pm$ 20 s), 12:59:55 ($\pm$ 30 s) and 13:08:20 ($\pm$ 30 s). The first and second pulse were therefore separated by 110–210 s. Loughlin *et al.* (2002) reports a reference density for the current of 1.6 kg m^{-3}, and we assume ambient air is at standard temperature and pressure (1.29 kg m^{-3}). Given these values we have a reduced gravity of $g' = 2.36 \text{ m s}^{-2}$. Finally, we must assign a characteristic length scale for the system as Loughlin *et al.* (2002) does not estimate the initial flow depth. We take the length scale to be in the range [500, 1000] m, as this is the order of magnitude of the flow depth of pyroclastic currents (Jones *et al.* 2023). A length scale of 500 m results in a buoyancy velocity of $U_b = 34.3 \text{ m s}^{-1}$, and a non-dimensional time delay between the first and second pulse in the range [7.55, 14.42], accounting for uncertainty in the release times. Taking a length scale of 1000 m results in a buoyancy velocity scale of $U_b = 48.55 \text{ m s}^{-1}$, and a non-dimensional time delay between the first and second pulse in the range [5.34, 10.20]. We investigate the dynamics of pulsed currents using an idealised experiment to allow careful study of the impact on front propagation relative to an instantaneous release for a wide range of non-dimensional delay times between pulses. Here, for simplicity, we use conservative flows as a proxy for non-conservative depositional flows (Meiburg *et al.* 2015).

There have been limited studies on pulsed gravity currents. Ho *et al.* (2018*a*) conducted lock-exchange experiments where two locks of length x_0 were released successively, with a non-dimensional delay time of $\tilde{t}_{re} = (t_{re} U_b)/x_0$ separating the release of the first and second lock, where t_{re} is the dimensional delay time. The results showed the second current propagated as an intrusion into the first and ultimately the pulses merged to form a unified
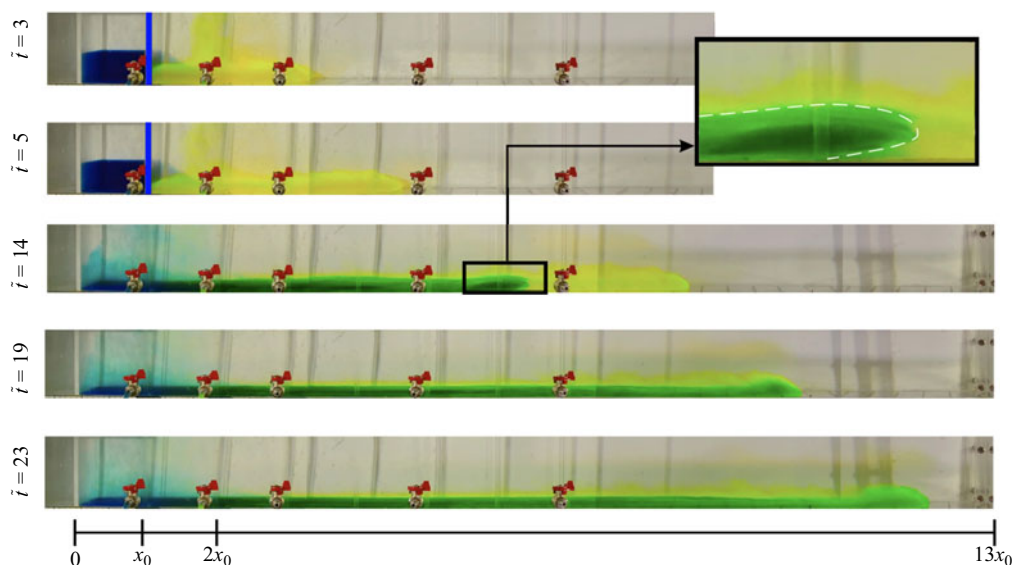
Figure 1. Visualisation of a sequential lock-box gravity current release (Ho *et al.* 2018*a*). In the experiments the lock-box length $x_0 = 0.125$ m, the initial current depth $h_0 = 0.05$ m, the second lock was released at $t_{re} = 4$ s and the buoyancy velocity scale $U_b = 0.1566$ m s^{-1}. Time is non-dimensionalised as $\tilde{t} = (tU_b)/x_0$, resulting in a non-dimensional release time of $\tilde{t}_{re} = 5$.

front, as can be observed in the visualisations of the experiments presented in figure 1. Ho *et al.* (2018*a*) also considered the implications for sedimentary deposits in turbidity currents, which was explored further by Ho *et al.* (2019). Ho *et al.* (2018*b*) conducted an analysis of the length scales of pulse merging. The pulsed gravity problem has similarities to the two-layer stratified locks, in that two gravity currents interact and mix over the lifetime of the flow (Dai 2017; Zhu, He & Meiburg 2023).

Methods used to numerically model idealised lock-gate releases can broadly be divided into two categories: depth-averaged models based on the shallow-water equations (SWEs) (Dorrell *et al.* 2014), and depth-resolving models based on the Navier–Stokes equations (Marshall *et al.* 2021). Numerical simulations of pulsed gravity currents were conducted by Allen *et al.* (2020), where the authors applied a depth-averaged SWE model to simulate the flow generated by a pulsed lock-exchange experiment, and explored pulsed flows for different regimes of $\tilde{t}_{re}$. Allen *et al.* (2020) showed that as $\tilde{t}_{re} \to \infty$ the pulses propagate as separate currents, and for $\tilde{t}_{re} < 1$ flow is equivalent to a single stage release of twice the volume, as the backwards travelling wave has yet to impact the second lock. For intermediate values of $\tilde{t}_{re}$, the second pulse advanced more rapidly than the first and ultimately merged with it, in agreement with the experimental findings. Allen *et al.* (2020) also observed that the speed of the second current at the time of merging was positively correlated with the delay time between releases. However, Allen *et al.* (2020) terminated simulations at the time of pulse merging. The front propagation of pulsed gravity currents after the currents merge, as a function of $\tilde{t}_{re}$, has not been studied.

The present study aims to address this open research question using the results of pulsed lock-exchange physical experiments, in combination with depth-averaged and depth-resolving numerical models. The research objectives are to investigate the front propagation of pulsed currents as a function of $\tilde{t}_{re}$ and elucidate the underlying dynamics.
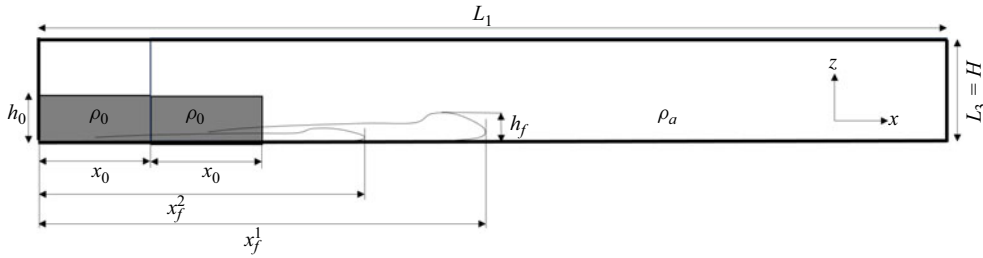
Figure 2. Schematic of dual-stage lock-exchange experiment.

2. Methods

The dynamics of pulsed gravity currents are investigated using physical experiments and numerical simulations, where the simulations include both depth-averaging and depth-resolving numerical models. We consider the dual-stage release lock-exchange problem. A schematic of the problem set-up and key parameters are presented in figure 2. The set-up consists of a straight channel of length L_1, width L_2 and height L_3. The channel contains two locks, each retaining a saline mixture of density ρ_0, separated from ambient fluid of density ρ_a. The density difference between the saline mixture and ambient fluid is small, $(\rho_0 - \rho_a)/\rho_a \ll 1$, hence the Boussinesq approximation can be applied. The initial depth of dense fluid is h_0, with the remaining channel depth $(L_3 - h_0)$ containing ambient fluid. Both locks have a length of x_0. The gates are released successively, with a delay time of $\tilde{t}_{re} = (t_{re} U_b / x_0)$ between the release of the first and second lock. The front location of the pulses generated by the first and second release are x_f^1 and x_f^2, respectively.

Thirty-three physical and numerical experiments quantifying dual-stage release flows are considered, the parameters for each case are presented in table 1. The physical experiments were conducted at a buoyancy Reynolds number of $Re_b \approx 6000$. The case list includes fractional depths of release of $h_0/L_3 \in \{10^{-5}, 0.1, 0.2, 0.5\}$. For each fractional depth of release we vary the non-dimensional delay time between the release of the first and second lock, $\tilde{t}_{re}$. As indicated in table 1, depth-averaged SWE simulations were conducted for Cases 1–27, physical experiments are run for Cases 13–18 and 25–27, and depth-resolving lattice Boltzmann method (LBM) simulations were run for Cases 25–33. The LBM simulations were run with a Reynolds number of $Re_b = 6000$. This allows the results of the physical experiments, SWE simulations and LBM simulations to be directly compared for Cases 25–27, where $h_0/L_3 = 0.5$. We are able to explore a wider parameter space with the SWE model due to its low computational cost relative to the depth-resolving LBM simulations.

2.1. *Physical experiments*

Physical experiments modelling pulsed-release lock-exchange gravity currents were conducted in a 5 m-long flume. At one end of the flume, two saline fluid regions of the same volume were contained in two lockboxes set up in series to model a pulsed current with two releases. The experimental set-up follows that of Ho *et al.* (2018*a*, 2018*b*) and Allen *et al.* (2020). Fluid in the two lockboxes were dyed yellow and blue to enable the visualisation of current mixing. The timing between two lock gates was set to vary between 0 s and 21.2 s using a pneumatic lock control box that ensured repeatability of both the timing and the speed of withdrawal of the lock. The density excess of the saline was 5 %. The height of the initial saline fluids and the length of each lock box were 0.05 m and 0.125 m, respectively. Ambient heights were set at 0.1 m and 0.25 m. The evolution of

Case	h_0/L_3	h_0/x_0	Re_b	$\tilde{t}_{re}$	Exp	Case run in SWE	LBM
1	10^{-5}	0.4	6000	0.25		✗	
2	10^{-5}	0.4	6000	5.13		✗	
3	10^{-5}	0.4	6000	11.02		✗	
4	10^{-5}	0.4	6000	14.41		✗	
5	10^{-5}	0.4	6000	27.94		✗	
6	10^{-5}	0.4	6000	42.61		✗	
7	0.1	0.4	6000	0.00		✗	
8	0.1	0.4	6000	5.13		✗	
9	0.1	0.4	6000	11.02		✗	
10	0.1	0.4	6000	14.41		✗	
11	0.1	0.4	6000	27.94		✗	
12	0.1	0.4	6000	42.61		✗	
13	0.2	0.4	5978	0.25	✗	✗	
14	0.2	0.4	6712	5.13	✗	✗	
15	0.2	0.4	6741	11.02	✗	✗	
16	0.2	0.4	5961	14.41	✗	✗	
17	0.2	0.4	5923	27.94	✗	✗	
18	0.2	0.4	6000	42.61	✗	✗	
19	0.5	0.4	6000	0.00		✗	
20	0.5	0.4	6000	5.13		✗	
21	0.5	0.4	6000	11.02		✗	
22	0.5	0.4	6000	14.41		✗	
23	0.5	0.4	6000	27.94		✗	
24	0.5	0.4	6000	42.61		✗	
25	0.5	0.4	6053	0.21	✗	✗	✗
26	0.5	0.4	6806	5.14	✗	✗	✗
27	0.5	0.4	6787	10.15	✗	✗	✗
28	0.5	1.0	6000	0.00			✗
29	0.5	1.0	6000	1.50			✗
30	0.5	1.0	6000	2.50			✗
31	0.5	1.0	6000	5.00			✗
32	0.5	1.0	6000	10.00			✗
33	0.5	1.0	6000	15.00			✗

Table 1. Case parameters for the dual-stage release lock-exchange study. The parameter space was investigated using a combination of physical experiments (Exp), depth-averaged SWE simulations and depth-resolving LBM simulations as indicated in the table.

flows was captured using two rail mounted high-definition cameras, tracking individual pulse fronts.

2.2. *Numerical modelling*

The macroscopic governing equations for a pulsed lock-exchange saline gravity current flow are those of mass and momentum conservation for an incompressible flow coupled, via the Boussinesq approximation, with an advection–diffusion equation for the scalar concentration field. Fluid density is defined as

$$\rho(\boldsymbol{x}, t) = \rho_a(1 + \alpha \chi(\boldsymbol{x}, t)), \tag{2.1}$$

where $\alpha = (\rho_s - \rho_a)/\rho_a$, ρ_s is solute density and $\chi(\boldsymbol{x}, t)$ is solute concentration. The body force generated by the action of gravity is $\boldsymbol{G}$,

$$\boldsymbol{G} = -g\rho_a(1 + \alpha \chi(\boldsymbol{x}, t))\hat{z}, \tag{2.2}$$

where $\hat{z}$ is the unit vector in the upward vertical direction. $\boldsymbol{G}$ includes a constant term that is the hydrostatic pressure term in the momentum equation, $\nabla P = \nabla(p_k(\boldsymbol{x}, t)) - g\rho_a z$, where p_k is the kinematic pressure. The driving force is the Boussinesq forcing term $\boldsymbol{F}_B$,

$$\boldsymbol{F}_B = -g\rho_a \alpha \chi(\boldsymbol{x}, t)\hat{z}. \tag{2.3}$$

The governing equations are non-dimensionalised using the characteristic length scale $h_0 = 0.05$ m, and velocity scale $U_b = 0.1566$ m s^{-1}, resulting in the non-dimensional incompressible mass and momentum conservation equations,

$$\nabla \cdot \tilde{\boldsymbol{u}} = 0, \tag{2.4}$$

$$\frac{\partial \tilde{\boldsymbol{u}}}{\partial \tilde{t}} + \tilde{\boldsymbol{u}} \cdot \tilde{\nabla}\tilde{\boldsymbol{u}} = -\tilde{\nabla}\tilde{P} + \frac{1}{Re_b}\tilde{\nabla}^2\tilde{\boldsymbol{u}} - \tilde{\chi}\hat{z} \tag{2.5}$$

and an advection–diffusion equation for the scalar concentration field $\tilde{\chi}$,

$$\frac{\partial \tilde{\chi}}{\partial \tilde{t}} + \tilde{\boldsymbol{u}} \cdot \tilde{\nabla}\tilde{\chi} = \frac{1}{Re_b Sc}\tilde{\nabla}^2\tilde{\chi}. \tag{2.6}$$

In addition to the buoyancy Reynolds number (Re_b) the governing equations are also parameterised by the Schmidt number $Sc = (\nu/D)$, where D is the diffusivity of the scalar field. All simulations are run with $Sc = 1$. The Schmidt number of real-world flows may be orders of magnitude larger, but the structure and dynamics of Boussinesq currents are relatively insensitive to Schmidt number for high Reynolds numbers of $\mathcal{O}(10^4)$ (Bonometti & Balachandar 2008; Marshall *et al.* 2021).

The concentration field is scaled relative to the initial saline concentration in the lock χ_0, i.e. $\tilde{\chi}, (\boldsymbol{x}, t) = \chi(\boldsymbol{x}, t)/\chi_0$. Fluid density is non-dimensionalised using the initial density of the current and ambient, such that $\tilde{\rho}(\boldsymbol{x}, t) = (\rho(\boldsymbol{x}, t) - \rho_a)/(\rho_0 - \rho_a)$. Variables with a ˜ accent are non-dimensionalised, and variables with a ¯ accent are the spanwise average of a non-dimensionalised variable, i.e.

$$\bar{\rho}(\tilde{x}, \tilde{z}, \tilde{t}) = \frac{1}{\tilde{L}_2}\int_0^{\tilde{L}_2} \tilde{\rho}(\tilde{x}, \tilde{y}, \tilde{z}, \tilde{t})\,\mathrm{d}\tilde{y}. \tag{2.7}$$

Here the macroscopic governing equations are not solved directly. We compare the use of: a depth-averaged model, implemented using the shallow-water approximation (§ 2.2.1); and a depth-resolving model, solving the governing equations at a mesoscopic scale, using a LBM model (§ 2.2.2).

2.2.1. *Depth-averaged shallow-water equations model*

In this section the methodology for an analytical SWE model is presented. Shallow-water models have extensively been used to study the lock-exchange problem as they exploit the small ratio between depth and length scales $\delta \sim h_f/x_f^1$. Consider a two-layered flow of immiscible fluids of thicknesses $h_1(x, t)$ and $h_2(x, t)$ and of similar, but distinct densities ρ_a and ρ_0, respectively, with $\rho_a < \rho_0$, figure 3. The flow is assumed to be symmetric in the cross-stream (y-direction) and the flow properties only vary over the direction of propagation x. Further, by assuming that the flows are inviscid, the depths h_i and depth-averaged velocities u_i for each layer are functions of (x, t) only. Surface tension and other intermolecular forces are assumed to be negligible. With the rigid-lid assumption total depth is $\mathcal{H}(x, t) = h_1 + h_2 = L_3$ and the the two-layer shallow-water model that was formulated by Rottman & Simpson (1983) can be applied. Using l_0 as the length scale,
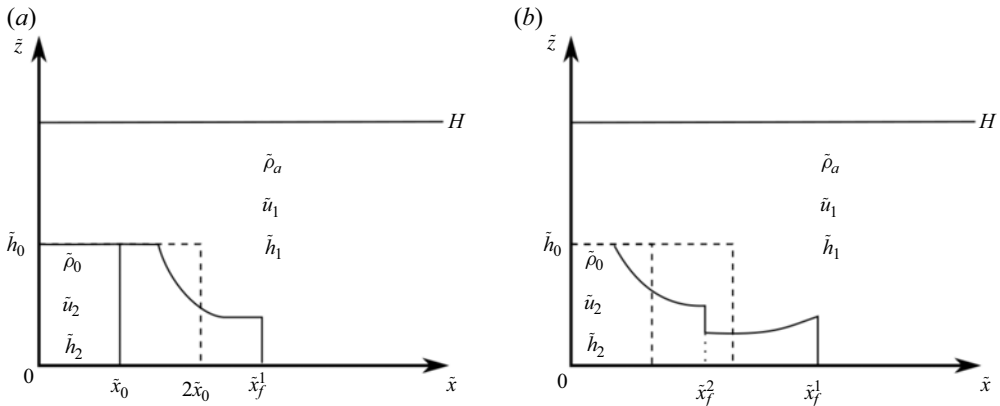
Figure 3. Double lock-release configuration for the shallow-water model: before the second gate release, (a) $\tilde{t} < \tilde{t}_{re}$, and after the second gate release, (b) $\tilde{t} > \tilde{t}_{re}$. The second release creates a shock in the solution which propagates forwards towards the head of the current. Horizontal and vertical lengths are non-dimensionalised by the lock-length l_{lock} and lock depth h_0, respectively. The position of the head is labelled $\tilde{x}_f^1$ and the second release that appears as a shock $\tilde{x}_f^2$.

h_0 as our depth scale, $\sqrt{h_0 g'}$ as the velocity scale and the convective time scale $\sqrt{h_0/g'}$, the dimensionless equations two-layer shallow-water equations are

$$\frac{\partial \tilde{h}}{\partial \tilde{t}} + \frac{\partial \tilde{m}}{\partial \tilde{x}} = 0, \qquad (2.8)$$

$$\frac{\partial \tilde{m}}{\partial \tilde{t}} + \frac{\tilde{m}}{\tilde{h}}(2 - 2a)\frac{\partial \tilde{m}}{\partial \tilde{x}} - \left(\frac{\tilde{m}^2}{\tilde{h}^2}(1 - 2a) - \tilde{h}(1 - b)\right)\frac{\partial \tilde{h}}{\partial \tilde{x}} = 0, \qquad (2.9)$$

where

$$a = \frac{\tilde{h}}{\tilde{L}_3 - \tilde{h}}, \qquad (2.10)$$

$$b = \frac{\tilde{h}}{\tilde{L}_3} + \frac{\tilde{m}^2}{\tilde{L}_3 \tilde{h}^2}\left(1 - \frac{\tilde{h}}{\tilde{L}_3}\right)^{-2}. \qquad (2.11)$$

Note that in the infinitely deep ambient limit, $\tilde{L}_3 \to \infty$ and $a, b \to 0$, the single-layer equations are recovered (Ungarish & Zemach 2005; Ungarish 2009). For flows in relatively deep $\tilde{L}_3 \gg 1$, the standard shallow-water equations can still be used and flow in the ambient neglected (Rottman & Simpson 1983; Hogg, Ungarish & Huppert 2000; Hogg 2006; Allen *et al.* 2020). However, as the ambient depth $\tilde{L}_3$ decreases the propagation speed of characteristic curves reduces, which leads to quantitative differences in the solution for lock-exchange gravity currents. For example, the duration of the slumping phase (where the head moves at constant speed) is increased (Rottman & Simpson 1983). The influence on the flow dynamics of the finite ambient depth increases as $\tilde{L}_3$ decreases until $\tilde{L}_3 < 2$, where the formation of a backwards propagating shock causes qualitative differences in the solution (Klemp, Rotunno & Skamarock 1994; Ungarish & Zemach 2005). The changing dynamics as $\tilde{L}_3$ decreases arise because of the increased work done by current accelerating the ambient fluid as it moves.

The initial and boundary conditions reflect a double lock-release and are equivalent to those used in Allen *et al.* (2020) to study dual-stage releases gravity currents in a infinitely

deep ambient,

$$\tilde{h}(\tilde{x}, 0) = \begin{cases} 1 & \text{if} \quad \tilde{x} \in [0, 2], \\ 0 & \text{otherwise}, \end{cases} \tag{2.12}$$

$$\tilde{u}(\tilde{x}, 0) = 0, \tag{2.13}$$

$$\frac{\partial \tilde{h}}{\partial \tilde{x}}(\tilde{x}_0, \tilde{t}) = 0 \quad \text{for} \quad \begin{cases} \tilde{x}_0 = 0, 1 & \text{for} \quad 0 \leqslant \tilde{t} < \tilde{t}_{re}, \\ \tilde{x}_0 = 0 & \text{for} \quad \tilde{t} > \tilde{t}_{re}, \end{cases} \tag{2.14}$$

where $\tilde{t}_{re}$ is the release time of the second lock box.

As discussed in the introduction, the moving head of the gravity current (right-hand boundary in this configuration) requires supplementation with a Froude number condition to accurately predict the propagation dynamics. The Froude number condition is expressed as a relationship between the depth $\tilde{h}_f$ and velocity $\tilde{u}_f$ at the head of the flow $\tilde{x} = \tilde{x}_f^1(t)$. At the head of the flow the dynamic boundary condition is also imposed giving

$$\frac{\mathrm{d}\tilde{x}_f^1}{\mathrm{d}\tilde{t}} \equiv \dot{\tilde{x}}_f^1 = \tilde{u}\left(\tilde{x} = \tilde{x}_f^1, t\right) = Fr\sqrt{\tilde{h}_f}, \tag{2.15}$$

where $\tilde{h}_f(\tilde{t}) = \tilde{h}(\tilde{x} = \tilde{x}_f^1, \tilde{t})$. In general the Froude number is a decreasing function of $\tilde{h}_f/\tilde{L}_3$ and many experimental or analytical expression exist for it (Benjamin (1968), Huppert & Simpson (1980), Rottman & Simpson (1983)). As $\tilde{L}_3 \to \infty$, the Froude number tends to a constant value and for deep ambient flows a constant value is taken (Hogg 2006; Allen *et al.* 2020). Ungarish & Zemach (2005) present a semiempirical formulation,
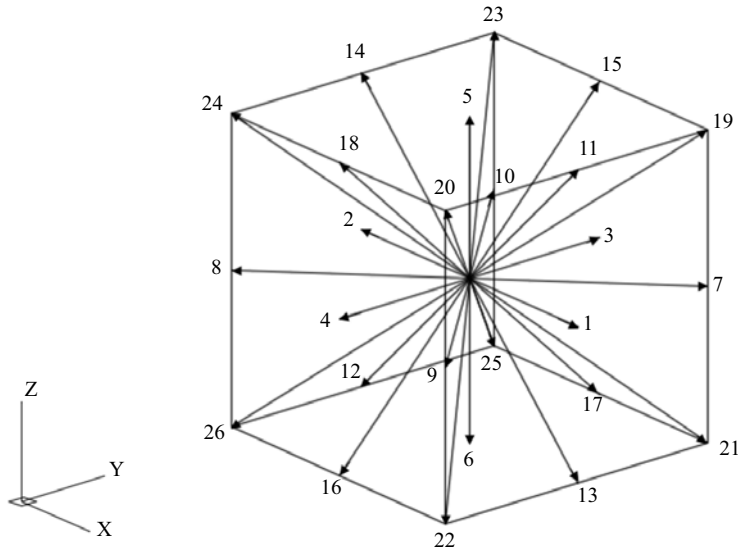
$$Fr\left(\frac{\tilde{h}_f}{\tilde{L}_3}\right) = Fr_{uz}\left(\frac{\tilde{h}_f}{\tilde{L}_3}\right)\left(1 + 3\frac{\tilde{h}_f}{\tilde{L}_3}\right)^{-1/2}, \tag{2.16}$$

as a compromise between other correlations whilst maintaining a reasonable agreement with a variety of experimental results. Crucially, the difference between these expressions is not particularly large in the region of shallow-water solutions $h_f/\tilde{L}_3 < 0.6$ (Ungarish & Zemach 2005). The present study is limited to the ranges $\tilde{L}_3 \geqslant 2$, or $\tilde{h}_f/\tilde{L}_3 < 0.5$. As $\tilde{L}_3 \to \infty$, $Fr_{uz} \to 1$. In addition to simulations conducted with $Fr = Fr_{uz}$, constant values of the Froude number Fr are also used for simulations with an infinitely deep ambient $\tilde{L}_3 \to \infty$.

To numerically solve the two-layer shallow-water model, ((2.8) and (2.9)) are mapped onto the unit interval [0, 1] using the transformation $(\zeta, \tau) = (\tilde{x}/\tilde{x}_f^1, \tilde{t})$. These scaled equations are solved using a Lax–Wendroff finite difference method similar to Bonnecaze, Huppert & Lister (1993), Ungarish & Zemach (2005) and Allen *et al.* (2020). A small artificial viscosity term is introduced using the formulation presented in Ungarish & Zemach (2005) to remove spurious oscillations that arise near large gradients and prevent the chequerboarding instability that arises with the Lax–Wendroff. For further details see Appendix A.

2.2.2. *Depth-resolving LBM model*

Depth-resolving simulations are produced by solving the macroscopic governing equations at the mesoscopic scale, i.e. between the macroscopic and microscopic scales, using the LBM (Krüger *et al.* 2017). The LBM simulations are run in VirtualFluids, an open-source

Figure 4. The $D3Q27$ lattice structure.

graphics processing unit accelerated code developed by the Institute for Computational Modelling in Civil Engineering (iRMB) at TU Braunschweig. Adekanye *et al.* (2022) validated VirtualFluids for the simulation of instantaneous release lock-exchange gravity currents with Reynolds numbers up to $Re_b = 30\,000$, showing good agreement with high-resolution simulations and physical experiments.

At the mesoscopic scale fluid motion is described by the particle distribution function (PDF) $f(\boldsymbol{x}, \boldsymbol{\xi}, t)$, where $\boldsymbol{\xi}$ is particle velocity. The PDF defines the density of particles at location $\boldsymbol{x}$, moving with velocity $\boldsymbol{\xi}$, at time t. The evolution of $f(\boldsymbol{x}, \boldsymbol{\xi}, t)$ is governed by the Boltzmann equation, which when discretised in space and time produces the lattice Boltzmann equation. In the present study we solve two two-way coupled lattice Boltzmann equations, one for the conservation of mass and momentum in the fluid,

$$f_{ijk}(\boldsymbol{x} + \boldsymbol{\xi}_{ijk}\Delta t, t + \Delta t) = f_{ijk}(\boldsymbol{x}, t) + \Omega_{ijk}^{f}(f_{ijk}, \Phi_{ijk}), \tag{2.17}$$

and a second for the advection and diffusion of the scalar concentration field,

$$\Phi_{ijk}(\boldsymbol{x} + \boldsymbol{\xi}_{ijk}\Delta t, t + \Delta t) = \Phi_{ijk}(\boldsymbol{x}, t) + \Omega_{ijk}^{\Phi}(\Phi_{ijk}, f_{ijk}). \tag{2.18}$$

Solving the system of lattice Boltzmann equations for the PDFs f_{ijk} and Φ_{ijk} is equivalent to to solving the macroscopic governing equations, (2.4)–(2.6) (Junk, Klar & Luo 2004; Dubois 2008). The equations are coupled via their respective collision operators, Ω_{ijk}^{f} and Ω_{ijk}^{Φ}.

The discretised PDF $f_{ijk}(\boldsymbol{x}, t)$, is defined at the nodes of a lattice structure in which lattice nodes are connected by a discrete velocity set $\boldsymbol{\xi}_{ijk}$. The indices i, j, k are permutations of the values $\{1, 0, -1\}$, and so $\boldsymbol{\xi}_{ijk}$ is a set of vectors to neighbouring nodes, which includes the zero vector. In the present study a $D3Q27$ lattice is used, which results in the lattice structure presented in figure 4. In effect, distributions are constrained to stream along the vectors $\boldsymbol{\xi}_{ijk}$ in time Δt, where they collide and are redistributed according to the collision operator Ω_{ijk}. The raw moments of a distribution, of order $\alpha + \beta + \gamma$, are defined as

$$m_{\alpha\beta\gamma}(\theta_{ijk}) = \sum_{i,j,k} i^{\alpha} j^{\beta} k^{\gamma} \theta_{ijk}. \tag{2.19}$$

The macroscopic fluid density and momentum density are recovered from the zeroth and first-order raw moments of f_{ijk},

$$\rho = m_{000} = \sum_{i,j,k} f_{ijk}, \tag{2.20}$$

$$\rho\boldsymbol{u} = \rho(m_{100}, m_{010}, m_{001} = \left(\sum_{i,j,k} i f_{ijk} + \frac{\Delta t}{2} F_B^x, \sum_{i,j,k} j f_{ijk} + \frac{\Delta t}{2} F_B^y, \sum_{i,j,k} k f_{ijk} + \frac{\Delta t}{2} F_B^z \right). \tag{2.21}$$

The zeroth raw moment of the Φ_{ijk} distribution gives the macroscopic concentration,

$$\chi = m_{000} = \sum_{i,j,k} \Phi_{ijk}. \tag{2.22}$$

Collisions for the f_{ijk} distribution are performed in cumulant space (Geier *et al.* 2015). Cumulants, C_{nrs}, are relaxed towards their equilibria C_{nrs}^{eq}, at a rate ω_{nrs},

$$C_{nrs}^* = (1 - \omega_{nrs})C_{nrs} + \omega_{nrs}C_{nrs}^{eq}. \tag{2.23}$$

The relaxation rate of the second-order cumulants determine the macroscopic fluid viscosity,

$$\nu = \frac{1}{3}\left(\frac{1}{\omega_{110}} - \frac{1}{2} \right) \frac{\Delta x^2}{\Delta t}. \tag{2.24}$$

Collisions for the Φ_{ijk} distribution are conducted in central moment space, using the method presented by Yang *et al.* (2016). The factorised central moments M_{nrs} are relaxed towards zero at the rate ω_{nrs},

$$M_{nrs}^* = (1 - \omega_{nrs})M_{nrs}. \tag{2.25}$$

The diffusivity of the scalar field is determined by the relaxation rate of the first-order factorised central moments,

$$D = \frac{1}{3}\left(\frac{1}{\omega_{100}} - \frac{1}{2} \right) \frac{\Delta x^2}{\Delta t}. \tag{2.26}$$

The dimensions of the computational domain are chosen to reflect the experimental conditions, with $L_1 = 27x_0$, and $L_2 = h_0$, resulting in a non-dimensional domain size of $\tilde{L}_1 = 27$, $\tilde{L}_2 = 1$, $\tilde{L}_3 = L_3/h_0$. Simulations are run on uniform meshes, with a spatial and time discretisation of $\Delta\tilde{x} = \Delta x/h_0 = 0.01$ and $\Delta\tilde{t} = 3 \times 10^{-4}$, respectively. The grid resolution is chosen such that the largest length scales of turbulent motion are directly resolved, whilst stability is maintained by limiting the relaxation rate of the third-order cumulant, as specified in the parameterised cumulant method of Geier, Pasquali & Schönherr (2017).

No-slip boundary conditions for the velocity field, and no-flux boundary conditions for the concentration field are applied to all external boundaries of the computational domain. These boundary conditions model the experimental set-up of the standard lock-exchange gravity current experiment, enabling direct validation against the observed front locations in the experimental results of Ho *et al.* (2018a).

The specific conditions for the $\tilde{x}_B$ boundary are defined as

$$
\begin{aligned}
\tilde{\boldsymbol{u}}(\tilde{\boldsymbol{x}} = (\tilde{x}_B, \tilde{y}, \tilde{z}), \tilde{t}) &= \mathbf{0} \\
\frac{\partial \tilde{\chi}}{\partial \tilde{x}}(\tilde{\boldsymbol{x}} = (\tilde{x}_B, \tilde{y}, \tilde{z}), \tilde{t}) &= 0
\end{aligned}
\quad \text{for} \quad
\begin{cases}
\tilde{x}_B = 0 \vee \tilde{x}_0 \vee \tilde{L}_1 & \text{for} \quad 0 \leqslant \tilde{t} < \tilde{t}_{re} \\
\tilde{x}_B = 0 \vee \tilde{L}_1 & \text{for} \quad \tilde{t} \geqslant \tilde{t}_{re}
\end{cases}.
\tag{2.27}
$$

A dual-stage release is achieved by inserting a no-slip and no-flux boundary condition on the yz-plane at $\tilde{x} = \tilde{x}_0$, which remains in effect until $\tilde{t} = \tilde{t}_{re}$, as shown in (2.27). The removal of this internal wall simulates the release of the second lock gate.

The no-slip and no-flux conditions for the $\tilde{y}_B$ and $\tilde{z}_B$ boundaries are defined as

$$
\begin{aligned}
\tilde{\boldsymbol{u}}(\tilde{\boldsymbol{x}} = (\tilde{x}, \tilde{y}_B, \tilde{z}), \tilde{t}) &= \mathbf{0} \\
\frac{\partial \tilde{\chi}}{\partial \tilde{y}}(\tilde{\boldsymbol{x}} = (\tilde{x}, \tilde{y}_B, \tilde{z}), \tilde{t}) &= 0
\end{aligned}
\quad \text{for} \quad \tilde{y}_B = 0 \vee \tilde{L}_2,
\tag{2.28}
$$

$$
\begin{aligned}
\tilde{\boldsymbol{u}}(\tilde{\boldsymbol{x}} = (\tilde{x}, \tilde{y}, \tilde{z}_B), \tilde{t}) &= \mathbf{0} \\
\frac{\partial \tilde{\chi}}{\partial \tilde{z}}(\tilde{\boldsymbol{x}} = (\tilde{x}, \tilde{y}, \tilde{z}_B), \tilde{t}) &= 0
\end{aligned}
\quad \text{for} \quad \tilde{z}_B = 0 \vee \tilde{L}_3.
\tag{2.29}
$$

No-slip and no-flux boundary conditions are implemented using the bounce-back method (Krüger *et al.* 2017).

The initial conditions of the computational domain are

$$
\tilde{\chi}(\tilde{\boldsymbol{x}}, \tilde{t}=0) = \begin{cases} 1 & \text{if} \quad \tilde{x} \leqslant 2\tilde{x}_0 \wedge \tilde{z} \leqslant \tilde{h}_0 \\ 0 & \text{otherwise} \end{cases},
\tag{2.30}
$$

$$
\tilde{\boldsymbol{u}}(\tilde{\boldsymbol{x}}, \tilde{t}=0) = 0.
\tag{2.31}
$$

These conditions align with the schematic of the dual-stage release experiment shown in figure 2. The initial and boundary conditions extend the methods used in Adekanye *et al.* (2022) to multistage releases. Adekanye *et al.* (2022) validate LBM models of single-stage releases against experimental data. Therefore, we expect that the initial and boundary conditions will provide sufficient accuracy to capture the dynamics of pulsed flows.

For the simulations of Cases 28–33 two passive scalars distributions are added to the simulation, Φ_{ijk}^{P1} and Φ_{ijk}^{P2}, which simulate the advection–diffusion of two scalar fields $\tilde{\chi}^{P1}$ and $\tilde{\chi}^{P2}$. The passive scalars are used to track the propagation and mixing of each release of dense material separately. The boundary conditions applied to the advection–diffusion simulations for $\tilde{\chi}^{P1}$ and $\tilde{\chi}^{P2}$ are the same as those applied to the $\tilde{\chi}$ scalar field in (2.27)–(2.29). The initial conditions for the passive scalar fields are defined such that $\tilde{\chi}^{P1} = 1$ in the first lock and is zero elsewhere, while $\tilde{\chi}^{P2} = 1$ in the second lock and is zero elsewhere,

$$
\tilde{\chi}^{P1}(\tilde{\boldsymbol{x}}, \tilde{t}=0) = \begin{cases} 1 & \text{if} \quad \tilde{x} \leqslant 2\tilde{x}_0 \wedge \tilde{x} > \tilde{x}_0 \wedge \tilde{z} \leqslant \tilde{h}_0 \\ 0 & \text{otherwise} \end{cases},
\tag{2.32}
$$

$$
\tilde{\chi}^{P2}(\tilde{\boldsymbol{x}}, \tilde{t}=0) = \begin{cases} 1 & \text{if} \quad \tilde{x} \leqslant \tilde{x}_0 \wedge \tilde{z} \leqslant \tilde{h}_0 \\ 0 & \text{otherwise} \end{cases}.
\tag{2.33}
$$

The passive scalars track the mixing of both pulses and can be used to determine the provenance of dense material at any time after the release of the lock gates.

Both the Φ_{ijk}^{P1} and Φ_{ijk}^{P2} are one-way coupled to the f_{ijk} distribution, so they are advected by the numerically calculated flow. The passive scalar distributions are solved for in an identical fashion to the two-way coupled distribution Φ_{ijk}, using (2.18). As the Peclet
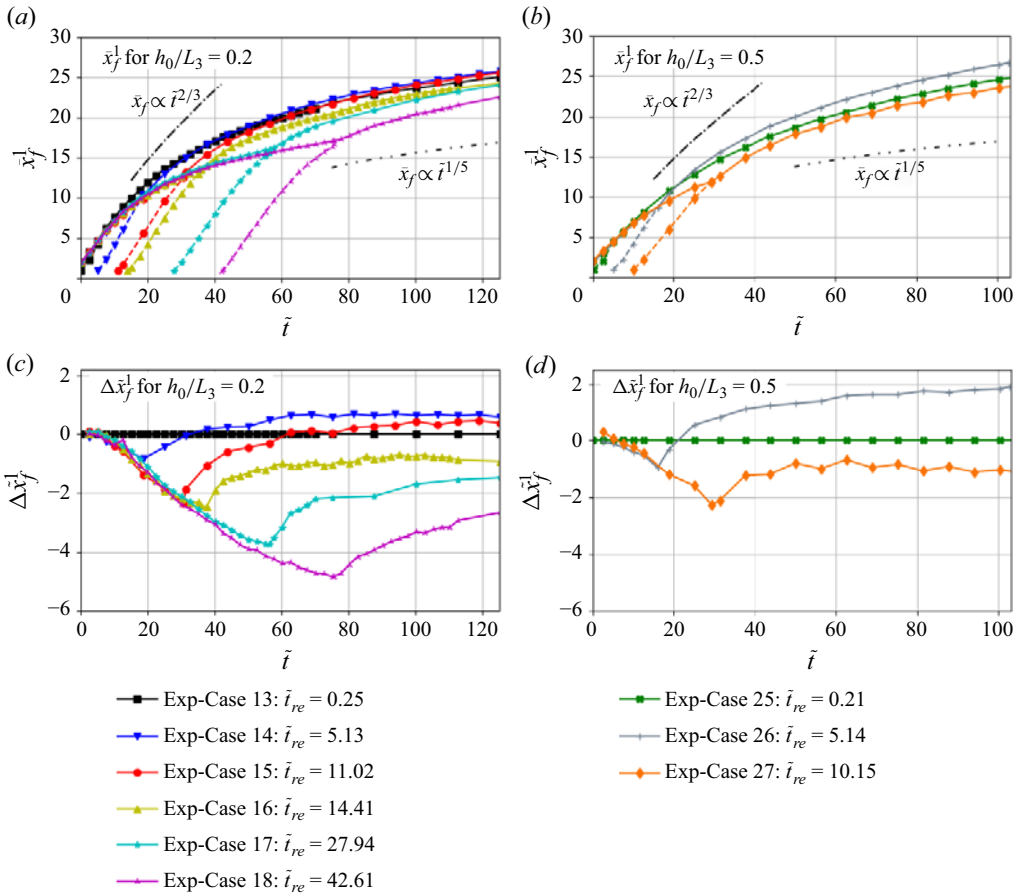
Figure 5. (*a*) Plots of front location of first pulse (x_f^1) in physical experiments (Exp) for $h_0/L_3 = 0.2$, Cases 13–18. (*b*) Plots of front location of first pulse (x_f^1) in physical experiments for $h_0/L_3 = 0.5$ Cases 25–27. (*c*) Plots of front location in physical experiments of Cases 13–18 relative to Case 13 ($\Delta \tilde{x}_f^1$). (*d*) Plots of front location in physical experiments of Cases 25–27 relative to Case 25 ($\Delta \tilde{x}_f^1$). The solid curves correspond to the front location of the current produced by the release of the first lock-gate, while the dashed lines track the front of the second pulse.

number ($Pe = Re_b Sc$) is large ($Pe \approx 6000$), we assume the impact of the diffusion term in (2.6) is negligible, hence $\tilde{\chi}(\boldsymbol{x}, t) \approx \tilde{\chi}^{P1}(\boldsymbol{x}, t) + \tilde{\chi}^{P2}(\boldsymbol{x}, t)$.

3. Results

3.1. *Physical experiments*

The front location of the gravity currents in Cases 13–18 and Cases 25–27 are presented in figure 5(*a*) and figure 5(*b*), respectively. The lock-exchange currents in Cases 13–18 have a fractional depth of release of $h_0/L_3 = 0.2$ and delay times $\tilde{t}_{re} \in [0.25, 42.61]$. Cases 25–27 have a fractional depth of release of $h_0/L_3 = 0.5$ and delay times $\tilde{t}_{re} \in [0.21, 10.15]$. The solid curves in figure 5 correspond to the front location of the current produced by the release of the first lock-gate, while the dashed lines track the front of the second pulse. When the pulses merge the dashed curve merges with the solid curve from the merge time

$\tilde{t}_M$ onwards. We observe a maximum variance in measured front location of $\sigma^2 = 0.19x_0$ across four repeats of physical experiments of Case 13.

The results for Cases 13 and 25, where $\tilde{t}_{re} \approx 0$, provide baselines against which to measure the impact of varying $\tilde{t}_{re}$. Cases 13 and 25 are single stage releases of a lock with dimensions $2\tilde{x}_0 \times \tilde{h}_0$. Within the slumping phase, where $\tilde{x}_f \propto \tilde{t}$, the current propagates with a buoyancy Froude number ($Fr_b = u_f / U_b$) of $Fr_b = 0.51$ in Case 13, and $Fr_b = 0.55$ in Case 25. This value is calculated by taking the mean velocity of the front for $\tilde{t} \leqslant 8$. After exiting the slumping phase the single stage release currents transition through the inertial phase and into the viscous phase. This is demonstrated in figure 5(*a,b*), where we observe the the current front locations briefly scaling like $\bar{x}_f \propto \tilde{t}^{2/3}$, before scaling like $\bar{x}_f \propto \tilde{t}^{1/5}$ at later times.

In Cases 14–18, where there is a delay between the release of the first and second lock, the current initially propagates as a single release of a lock with dimensions $\tilde{x}_0 \times \tilde{h}_0$. The release of the second lock gate generates a dense intrusion into the leading gravity current. The pulses ultimately merge to form a unified front, as seen in figure 1. The merging time corresponds to an inflection point in the solid curve tracking the front location of the leading current. This is due to the acceleration of the front relative to its velocity immediately prior to the time of merging. The same trends are observed in Cases 25–27, where Case 25 is the baseline case ($\tilde{t}_{re} = 0.25$) against which Cases 26 and 27 are compared. Although both lock gates in Cases 13 and 25 are released simultaneously, there is still a non-zero merging time due to the transit time for the downstream buoyancy-flux in the inner region of the body to transport dense material to the head of the current.

The findings here are best illustrated through plots of the relative front location of each pulsed current ($\tilde{t}_{re} > 0$) compared with a single release of an equal volume of dense fluid, i.e. the $\tilde{t}_{re} \approx 0$ case with equivalent parameters. The relative displacement between the front of a single and pulsed release is defined as

$$\Delta \tilde{x}_f^1(\tilde{t}, \tilde{t}_{re}) = \tilde{x}_f^1(\tilde{t}, \tilde{t}_{re}) - \tilde{x}_f^1(\tilde{t}, \tilde{t}_{re} = 0). \tag{3.1}$$

Plots of relative front location ($\Delta \tilde{x}_f^1$) against time are presented in figures 5(*c*) and 5(*d*) for Cases 13–18 and Cases 25–27, respectively. These are plots of front location in a frame of reference moving with the front of the single release currents.

The same trends are observed in both sets of results. For the benchmark cases, Cases 13 and 25 where $\tilde{t}_{re} \approx 0$, the $\Delta \tilde{x}_f^1$ curve is identically zero for all $\tilde{t}$ by definition. Several clear trends emerge when comparing the front position of pulsed currents with their respective benchmarks. At early times the relative front location is negative, $\Delta \tilde{x}_f^1 < 0$. This distance continues to grow until the merge time of each pulsed current. At the merge time there is an inflection point in the $\Delta \tilde{x}_f^1$ curves, and the unified fronts of the pulsed gravity currents accelerate relative to the front of the single release current. The relative acceleration of the pulsed flows does not continue indefinitely, ultimately the acceleration slows and the relative front position plateaus at a constant value. At late times the unified front propagates under the viscous scaling law, $\bar{x}_f \propto \tilde{t}^{1/5}$.

The key result is that for pulsed currents with relatively short delay times – specifically $\tilde{t}_{re} \in \{5.26, 11.02\}$ in figure 5(*c*), and $\tilde{t}_{re} = 5.14$ in figure 5(*d*) – the front of the pulsed current accelerates beyond the velocity of a single release current and plateaus at a value $\Delta \tilde{x}_f^1 > 0$. This in contrast to the pulsed currents with longer delay times, where the phase of relative acceleration ends before the current velocity exceeds that of the single release current, and relative front location plateaus at a value $\Delta \tilde{x}_f^1 < 0$.

In summary, the physical scale experiments show that when varying the delay time between the release of two lock-gates in a pulsed gravity current experiment, there

exists a range of short delay times that generate a current that propagates faster than an instantaneous release of an equivalent volume of dense material. Additionally, relatively long delay times between releases results in a current that propagates slower than an equivalent instantaneous release. We are unaware of this result being published previously in the gravity current literature, yet the findings could impact the conventional understanding of how gravity currents propagate in a range of environmental contexts.

The experimental results give rise to a series of research questions that will be addressed in the remainder of this study. Firstly, are depth-averaging models, typically used for geohazard assessment, capable of capturing the observed phenomena, and how do they perform relative to depth-resolving models? Secondly, what are the physical mechanisms that result in pulsed releases, with short delay times, generating faster currents than an equivalent instantaneous release?

3.2. *Validation of numerical simulations against physical experiments*

Front propagation results from physical experiments, depth-averaged SWE model simulations and depth-resolving LBM simulations of Cases 25–27 are presented in figure 6. The results for the benchmark single release case, Case 25 where $\tilde{t}_{re} = 0.1$, are presented in figure 6(*a*). Here we quantify the error in numerical predictions relative to experimental data through the mean absolute percentage error (MAPE),

$$\text{MAPE} = \frac{100}{n} \sum_{i=1}^{n} \left| \frac{\bar{x}_{f,ex}^1(\tilde{t}_i) - \bar{x}_{f,num}^1(\tilde{t}_i)}{\bar{x}_{f,ex}^1(\tilde{t}_i)} \right|, \tag{3.2}$$

where n in the number data points in an experimental time series consisting of the discrete times $\tilde{t}_i$, $\bar{x}_{f,ex}^1$ is the experimentally observed spanwise averaged current front location and $\bar{x}_{f,num}^1$ is the numerically predicted spanwise averaged front location.

Good agreement between the LBM predictions and the experimental results is observed for Case 25, throughout the slumping, inertial and viscous phases. The LBM model achieves an MAPE of 6.6 % in predictions of $\bar{x}_f^1$ in the time range $\tilde{t} \in [0, 90]$, and a relative error of 5.1 % for observation at $\tilde{t} = 88$. The capability of the LBM model to simulate the front propagation of single release currents is thoroughly validated by Adekanye *et al.* (2022).

The depth-averaged SWE model shows good agreement with the physical experiment in the slumping phase, but diverges at later times when the current produced by the physical experiment enters the viscous phase. This is due to the assumption of inviscid flow in the shallow-water equations, which means that viscous forces are not captured in the simulations. Therefore, the depth-averaged model never enters the viscous phase. This can be observed in figure 6(*a*), where the evolution of front location with respect to time remains close to the inviscid scaling law of $\bar{x}_f \propto \tilde{t}^{2/3}$ at late times. The SWE model achieves an MAPE of 14.9 % in predictions of $\bar{x}_f^1$ in the time range $\tilde{t} \in [0, 90]$, more than twice the LBM model's MAPE. Additionally, the SWE model has an error of 34.7 % relative to the experimental observation at $\tilde{t} = 88$, which is significantly larger than the LBM error.

The results for the pulsed currents are presented in figures 6(*b*) and 6(*c*) for Case 26 and Case 27, respectively. As in Case 25, the LBM simulations, SWE model and experiments are in very close agreement in the slumping phase of the flow.

The merge times for the physical experiments of Cases 26 and 27 were measured and determined to be $\tilde{t}_M = 16.10$ and $\tilde{t}_M = 29.34$, respectively. The merge times predicted by the LBM and SWE models are in good agreement with the experimental results.
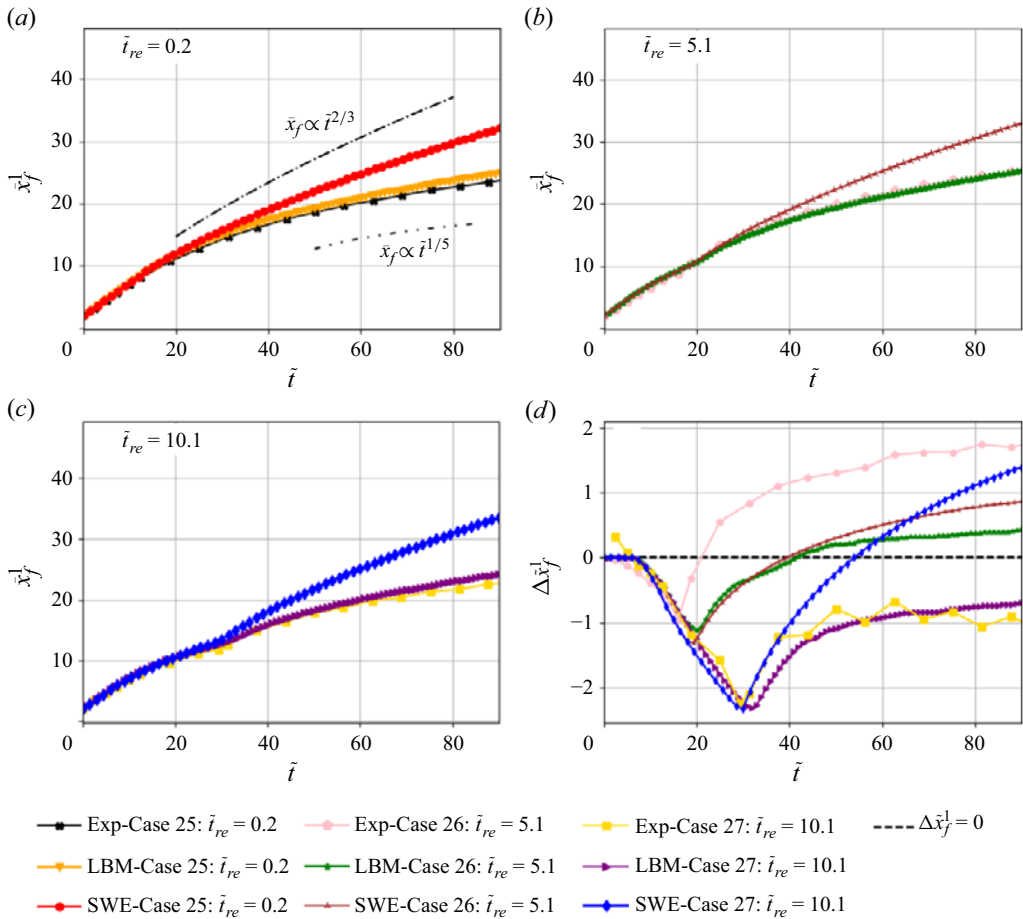
Figure 6. Plots of head location in the experiments, depth-averaged SWE model and depth-resolving LBM simulations of (*a*) Case 25, $\tilde{t}_{re} = 0.2$, (*b*) Case 26, $\tilde{t}_{re} = 5.1$, (*c*) Case 27, $\tilde{t}_{re} = 10.1$. (*d*) Plots of head location of the leading currents relative to their respective baseline single stage release case ($\Delta \tilde{x}_f^1$) in experiments, depth-averaging and depth-resolving simulations of Cases 25–27.

The merge times in the numerical simulations can be effectively approximated as the time corresponding to the inflection point in the front location curve. The inflection point is caused by the second pulse transferring energy to the first, causing a relative acceleration in front velocity. The LBM model predicts merge times for Cases 26 and 27 of $\tilde{t}_M = 20.0$ and $\tilde{t}_M = 32.0$, respectively, while the SWE model predicts merge times of $\tilde{t}_M = 19.5$ and $\tilde{t}_M = 30$, respectively.

Prior to the experimentally measured merge times for Case 26 and 27, the LBM model achieves MAPE metrics of 12.2 % and 8.1 %, demonstrating good quantitative agreement with the experimental data. After the currents merge, the LBM simulations continue to accurately simulate front propagation, maintaining close agreement with the experiments into the viscous phase. The LBM model achieves an MAPE of 1.9 % and 4.3 % in predictions of $\bar{x}_f^1$, for the time period $\tilde{t} \in [\tilde{t}_M, 90]$, in Cases 26 and 27, respectively. The LBM model also demonstrates close agreement with the experimental front location observation at $\tilde{t} = 88$; with relative errors of 0.4 % and 6.1 % in Cases 26 and 27. The LBM MAPE score for the full time series, $\tilde{t} \in [0, 90]$, is 5.7 % and 5.9 % for Cases 26 and 27.

The SWE model shows close agreement with the experimental data prior to current merging, achieving MAPE scores of 6.0 % and 4.1 % for the period $\tilde{t} \in [0, \tilde{t}_M]$ in Cases 26 and 27, respectively. However, as initially observed in Case 25, the predictions of the SWE model diverge from the LBM model and experiments at later times due to the absence of viscous effects. Basal drag could be included in the model to capture some of the viscous effects felt by the current during the slumping and inertial phases of the flow, for example Hogg & Pritchard (2004). However, Johnson & Hogg (2013) show that the overall effect of basal drag is often limited for turbulent flows. Once the current has transitioned to the viscous phase, the constant velocity profile over the depth of the current breaks down and the depth-averaged model is no longer applicable. Furthermore, the SWE model does not include the entrainment of ambient flow. Shallow-water models have been extended to include entrainment by Johnson & Hogg (2013) who demonstrate that entrainment becomes increasingly important over time for inertial gravity currents, and an entraining regime exists inbetween the inertial and viscous phases if the current is not small and does not transition immediately from the inertial to viscous regime. In this entraining regime $\bar{x}_f \propto \tilde{t}^{0.447}$. The head position in figure 6(*a*) demonstrates when the SWE is travelling too fast, the current is already in the viscous regime. Johnson & Hogg (2013) indicate that the entraining regime may be difficult to observe at laboratory scale, but a three-equation model would be more suitable to large-scale flows if entrainment is important. As a result of these limitations the SWE model predictions of $\bar{x}_f^1$ have an MAPE of 13.7 % and 27.9 %, for the time period $\tilde{t} \in [\tilde{t}_M, 90]$, in Cases 26 and 27, respectively. Additionally, the viscous phase divergence results in large errors for the SWE model at $\tilde{t} = 88$; with relative errors of 28.9 % and 46.0 % in Cases 26 and 27, respectively. The SWE MAPE score for the full time series, $\tilde{t} \in [0, 90]$, are 11.2 % and 17.8 % for Cases 26 and 27.

The key finding in the results of the physical experiments was that a delay time of $\tilde{t}_{re} = 5.1$ (Case 26) resulted in a current that propagated faster than an instantaneous release (Case 25) after the fronts merged, while a delay time of $\tilde{t}_{re} = 10.1$ (Case 27) resulted in a slower current after the fronts merged. Plots of relative front location $\Delta \tilde{x}_f^1$ for Cases 25–27 taken from results of the physical experiments, depth-averaged SWE simulations, and depth-averaged LBM simulations are shown in figure 5(*d*). The results show that the LBM simulations successfully reproduce the trends observed in the physical experiments. Prior to the merge time $(\tilde{t}_M)$ the front location of the pulsed currents falls behind the single release current, i.e. $\Delta \tilde{x}_f^1 < 0$. At $\tilde{t} = \tilde{t}_M$ there is an inflection in the relative front location curve, and both pulsed currents accelerate relative the single release current. In the LBM simulation of Case 27, the model correctly predicts that relative front location plateaus at a negative value, $\Delta \tilde{x}_f^1 < 0$. The model accurately captures the relative acceleration of Case 26, with relative front location increasing and ultimately plateauing at a positive value, $\Delta \tilde{x}_f^1 > 0$. The SWE model does not predict that short delay times between releases generate faster currents than in instantaneous release, while longer delays result in slower currents. Instead, the SWE model predicts that both the $\tilde{t}_{re} = 5.1$ and $\tilde{t}_{re} = 10.1$ currents accelerate beyond the baseline current after the fronts have merged. Additionally, the SWE model predicts that the relative acceleration of pulsed current increases with larger delay times.

3.3. *Depth-averaged model*

The two-dimensional depth-averaged SWE model was used to simulate the conditions recorded for the physical scale experiments. The SWE model is used to capture both the front position and the variation in flow velocity and depth along the length of the flows.
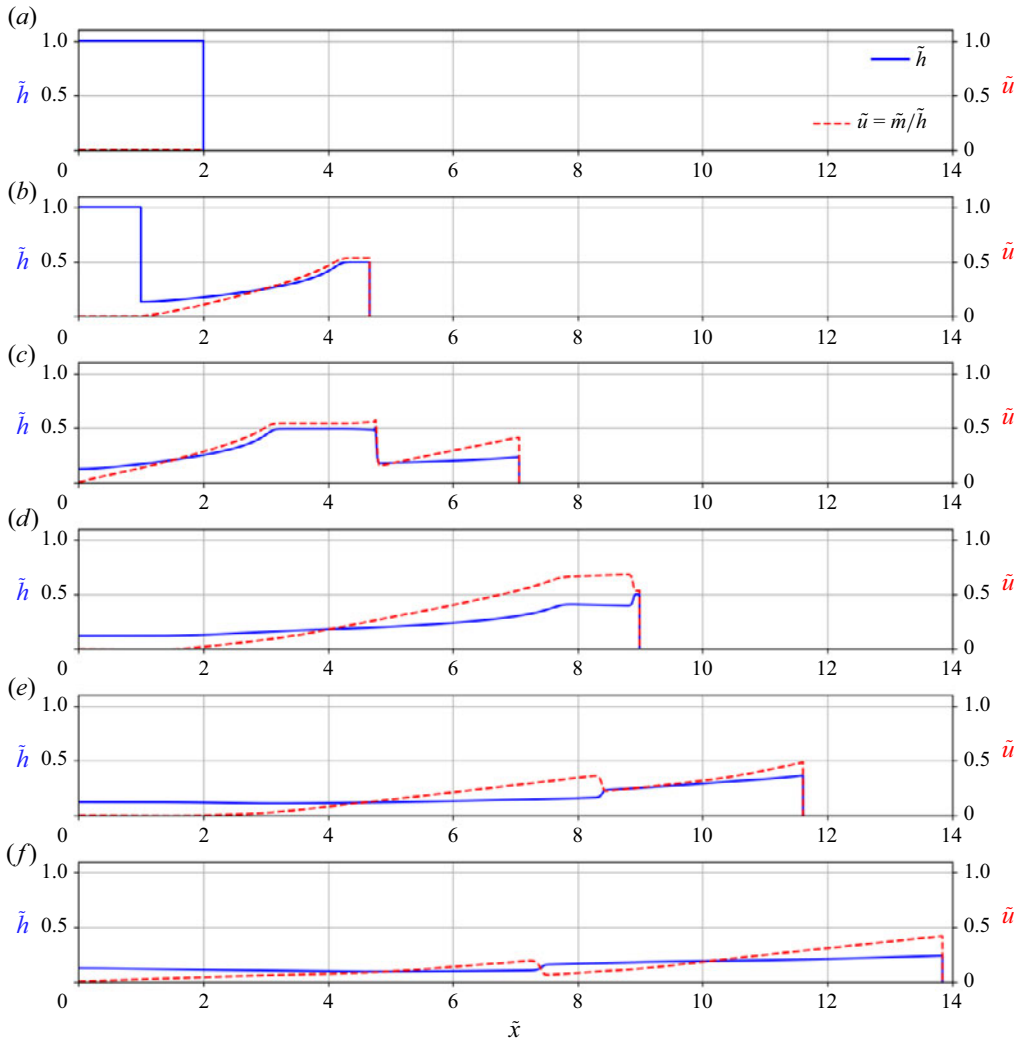
Figure 7. Depth and horizontal velocity profiles from the depth-averaged shallow-water model. The ambient depth is $\tilde{L}_3 = 2$, the second gate release time is $\tilde{t}_{re} = 5.13$ and the $Fr = Fr_{uz}(h_f/L_3)$ condition is imposed at the head of the flow. Panel (a) corresponds to the initial conditions ($\tilde{t} = 0$). Subsequent panels increase in uniform time intervals and from (b) to (f) correspond to $\tilde{t} = 5, 10, 15, 20, 25$. Small oscillations can be observed behind the shock as it propagates forwards to the head of the current but these dissipate once the shock reflects from the head.

3.3.1. *Visualisation of results*

Example flow dynamics are presented for Case 20 at six different times in figure 7. These simulations have a finite ambient depth of $\tilde{L}_3 = 2$ and a dimensionless release time of $\tilde{t}_{re} = 5.13$. The Froude number condition proposed by Ungarish & Zemach (2005), $Fr = Fr_{uz}(\tilde{h}_f/L_3)$, is used at the front boundary condition. The first release propagates forward as gravity current. Between the $\tilde{t} = 5$ and $\tilde{t} = 10$ plots, the second gate is released. Because the fluids are of equal density releasing the second lock gate generates a shock, recognised as a forward propagating wave, that propagates towards the head of the flow. Numerical instabilities result in small oscillations behind the shock. These instabilities are suppressed
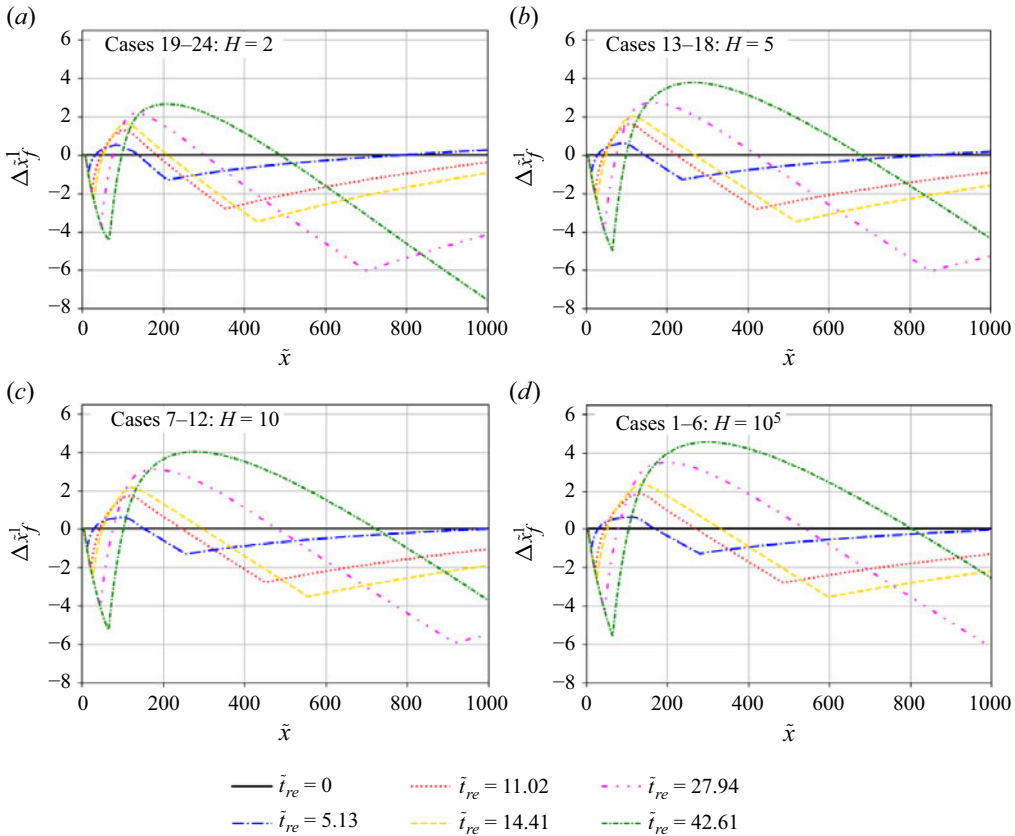
Figure 8. Depth-averaged shallow-water model predictions of head displacement for dual-stage release flows relative to a single release of the same volume of material as the ambient depth increases: (*a*) Cases 19–24 ($\tilde{L}_3 = 2$); (*b*) Cases 13–18 ($\tilde{L}_3 = 5$); (*c*) Cases 7–12 ($\tilde{L}_3 = 10$); (*d*) Cases 1–6 ($\tilde{L}_3 = 10^5$). The depth dependent Froude number $Fr_{uz}(h_f/\tilde{L}_3)$ is used to determine the head speed of the current.

by an artificial viscosity, as detailed in Appendix A. The shock arrives at the head after $\tilde{t} = 15$ and a backwards travelling shock is then observed in the $\tilde{t} = 20$ plot.

3.3.2. *Head position relative to a single release for finite depth ambient*
In this section the SWE model head position predictions for an instantaneous release and pulsed currents are compared. For a given Froude number condition, the position of the head of a dual-stage release is a function of time and dependent on the parameter $\tilde{t}_{re}$, i.e. $\tilde{x}_f^1 = \tilde{x}_f^1(\tilde{t}, \tilde{t}_{re})$. The instantaneous release simulations (of twice the material) is run as a sequential release simulation with $t_{re} = 0$. Theoretically, any value of $\tilde{t}_{re}$ less than 1 will work for all $\tilde{L}_3$ in a shallow-water type model as this is the time for the backwards travelling wave to reach the back of the first lock box.

The relative displacement between instantaneous and pulsed current head positions Δx_f^1 is displayed in figure 8 for Cases 1–24, which span four different ambient depths, $\tilde{L}_3 = 2, 5, 10$ and $100\,000$, and different second gate release times. The values $\tilde{L}_3 = 2$ and $\tilde{L}_3 = 5$ are chosen to match the experimental results. Here $\tilde{L}_3 = 100\,000$ is chosen to approximate an infinite ambient depth release for verification with the single-layer shallow-water equations model of Allen (2018). Finally, the value $\tilde{L}_3 = 10$ enables us to

see the transitional behaviour as $\tilde{L}_3$ becomes large. Until the reflection of the backwards travelling wave reaches the head of the flow, all currents travel at the same speed. After this time, $\tilde{t} \approx 5$, the double release head speed reduces and $\Delta \tilde{x}_f^1$ decreases for all phased release cases. The arrival of the shock at the head of the current signifies a rapid acceleration of the head of current and hence $\Delta \tilde{x}_f^1$ increases. Critically, in contrast to the experiments and the LBM, $\Delta \tilde{x}_f^1$ reaches a maximum value, which is greater than zero, after this point for phased releases. This means that the phased-released flows have travelled further at the point in time.

3.3.3. *Characteristic diagrams for infinite depth release*

If the infinite depth limit, $\tilde{L}_3 \to \infty$, is considered, then the two-layer shallow-water equations reduce to the single-layer equations, where Riemann invariants exist (Hogg 2006; Allen *et al.* 2020). Further, the Froude number tends to a constant value. The correlation proposed by Ungarish & Zemach (2005) Fr_{uz} and used in this study tends to 1 as $\tilde{L}_3 \to \infty$. However, different correlations have different limits. For example, the Benjamin condition tends to $\sqrt{2}$ (Benjamin 1968). Allen *et al.* (2020) identified three key curves based on the characteristics whose interaction with the shock qualitatively changes the solution and, in particular, the shock propagation speed for phased release flow in an infinitely deep ambient. The positive and negative characteristic curves for the infinite depth SWE are

$$\frac{dx}{dt} = u + \sqrt{h}, \tag{3.3}$$

$$\frac{dx}{dt} = u - \sqrt{h}, \tag{3.4}$$

respectively, with corresponding Riemann invariants $\alpha = u + 2\sqrt{h}$ and $\beta = u - 2\sqrt{h}$ and require numerical integration for certain flow regions. The first two, $\tilde{x}_{ref}$ and $\tilde{x}_{fan}$, emanate from the front of the first lock box, $(\tilde{x}, \tilde{t}) = (2, 0)$, and initially correspond to the fastest and slowest moving negative characteristics that bound an expansion fan that describes the decreasing flow depth behind the head. Until reaching the back of the first lock box x_{ref} corresponds to the backwards travelling disturbance propagating into undisturbed fluid, i.e. $\tilde{h} = 1$ to the left of $\tilde{x}_{ref}$. At $\tilde{t} = 1$, $\tilde{x}_{ref}$, the backwards travelling disturbance, reflects of the back of the first lock box and follows the path of the last positive characteristic emanating from unperturbed fluid. The reflected wave propagates towards the head of the flow and when it reaches the head the slumping phase finishes. During the slumping phase, the head of the current has not been affected by the finite supply of material within the lock box and moves with constant speed and depth. After this, $\tilde{x}_{ref}$, tracks the subsequent reflections of this curve and switches polarity back and forth as it reaches either the head or the back of the lock box. The second curve $\tilde{x}_{fan}$ initially bounds the region where the solution changes from uniform (constant depth) to simple (varying depth). Both these curves influence the propagation speed of the shock. Similarly to $\tilde{x}_{ref}$, the fastest backwards propagating characteristic from the second release and its subsequent reflections is also tracked as the curve $\tilde{x}_{fan}$. A curve similar to $\tilde{x}_{ref}$, which tracks the backwards travelling disturbance from the second lock box is also introduced and labelled $\tilde{x}_{fin}$. The position of the second release $\tilde{x}_s$, which appears as a shock, and its subsequent reflections is also tracked. The shock corresponds to a location where characteristics in one of two directions intersect. In particular any of the three curves discussed above would follow the path of the shock after reaching it when representing a characteristic in the same direction as the shock.
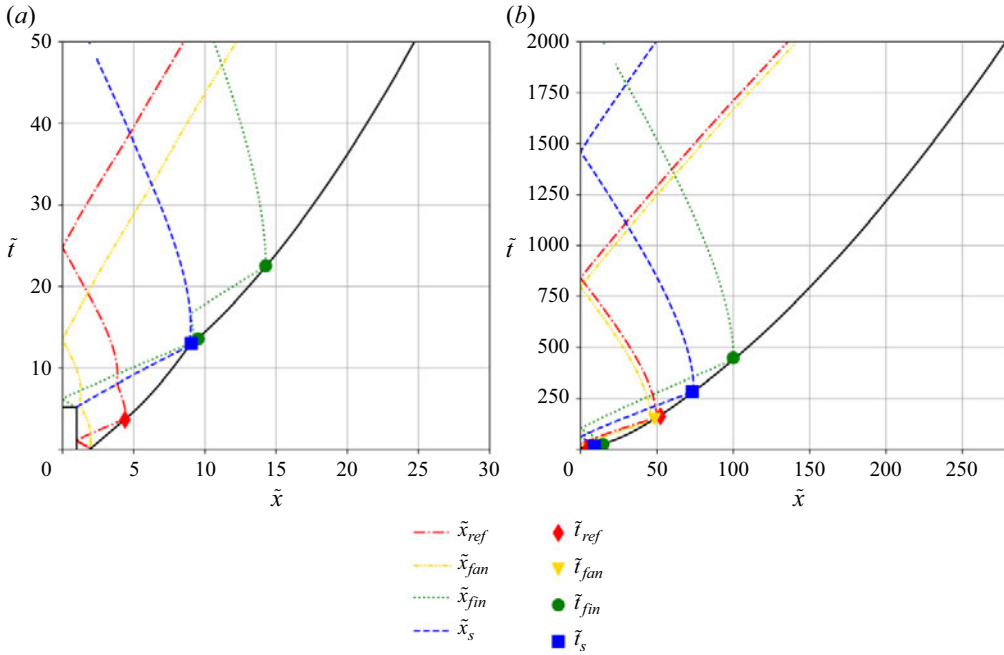
Figure 9. Characteristic diagrams showing the key curves: $\tilde{x}_{ref}$, $\tilde{x}_{fan}$, $\tilde{x}_{fin}$, $\tilde{x}_s$ and the head of the current $\tilde{x}_f^1$ for Case 2; $\tilde{t}_{re} = 5.13$, $\tilde{L}_3 \to \infty$ and $Fr = 1$. The times $t_{ref}(\blacklozenge)$, $t_{fin}(\bullet)$, $t_s(\blacksquare)$ and $t_{fan}(\blacktriangledown)$ indicate when the key characteristic curve or the shock intersects the head of the flow. This is to highlight the change in relative head position in figure 11. This corresponds to a $C_1 Ni$ case identified by Allen *et al.* (2020). Panel (*a*) shows the early stages of the flow $\tilde{t} < 50$.

The change in characteristics arriving at the shock will change the shock propagation speed and hence the value of the other characteristic, which naturally travels back from the shock. To track this change, if any of $\tilde{x}_{ref}$, $\tilde{x}_{fan}$ or $\tilde{x}_{fin}$ reach the shock they then switch to following a characteristic of the opposite polarity.

Diagrams of the four key curves based on characteristics, $\tilde{x}_{ref}$, $\tilde{x}_{fan}$, $\tilde{x}_{fin}$ and $\tilde{x}_s$, and the front flow boundary $\tilde{x}_f^1$ are plotted in figure 9 for Case 2; $Fr = 1$, $\tilde{t}_{re} = 5.13$ and $\tilde{L}_3 \to \infty$. This case corresponds to a $C_1 Ni$ shock identified by Allen *et al.* (2020). Initially, the shock propagates at constant speed before intersecting $\tilde{x}_{fan}$ and then $\tilde{x}_{ref}$ before reaching the head. Over the total integration time $\tilde{t}_{int} = 1000$, the shock $\tilde{x}_s$, in addition to $\tilde{x}_{ref}$ and $\tilde{x}_{fan}$, reflects off the head of the current, off the back of the lock box and then again reach the head of the flow. These intersection times with the head of the flow are labelled $\tilde{t}_{ref}$, $\tilde{t}_{fan}$, $\tilde{t}_{fin}$ and $\tilde{t}_s$ and also displayed in figure 9. When comparing the relative displacement between single and double releases, Δx_f^1, these curves highlight some of controls on whether the double release is travelling faster or slow than the single release, figure 10. Each minimum of $\Delta \tilde{x}_f^1$ occurs when the shock or its reflection reaches the head of the flow. In between each of these minima, $\Delta \tilde{x}_f^1$ increases to a maximum that is larger than zero, before decreasing again. None of the other points correspond to an extrema in $\Delta \tilde{x}_f^1$. However, numerous coincide with changing behaviour in $\Delta \tilde{x}_f^1$. For example, at $\tilde{t} \approx 175$ for $\tilde{t}_{re} = 5.13$ the gradient increases after $\tilde{t}_{fan}$ and $\tilde{t}_{ref}$ in quick succession. This is to be expected as they indicate changing behaviour in the positive characteristics arriving at the
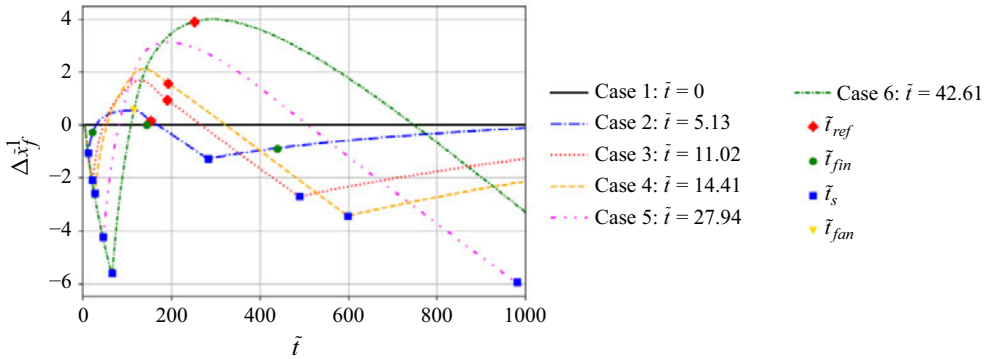
Figure 10. Relative displacement between single and phased releases ($\Delta\tilde{x}_f^1$) for Cases 1–6, which approximate an infinitely deep ambient ($\tilde{L}_3 \to \infty$). The times $t_{ref}(\blacklozenge)$, $t_{fin}(\bullet)$, $t_s(\blacksquare)$ and $t_{fan}(\blacktriangledown)$, indicate when the key characteristic curve or the shock intersects the head of the flow. The first occurrence of t_{fan}, t_{ref} and t_{fin} are suppressed for clarity.

head (Allen *et al.* 2020). The change in gradient of $\Delta\tilde{x}_f^1$ is also observed in the finite depth cases, figure 8, for $\tilde{L}_3 = 10$ and $\tilde{L}_3 = 5$.

In addition to $Fr = 1$, two more studies are conducting using $Fr = 0.9$ and $Fr = 1.1$ for Cases 1–6. The characteristic diagrams appear similar to figure 9. The relative displacement between single and double release for each of these is plotted in figure 11. Lower Froude numbers result in a lower propagation speed of the current and hence, the shock $\tilde{x}_s$ has less distance travel between the head of the current and the back of the lock box. Thus, the time between minima and maxima of $\Delta\tilde{x}_f^1$ decreases. The decreased propagation speed and time between extrema results in the magnitude of extrema in $\Delta\tilde{x}_f^1$ being smaller. As $Fr_{uz} \to 1$ and $\tilde{h}_f/\tilde{L}_3 \to 0$, the long-term behaviour for $Fr = Fr_{uz}$ is similar to the $Fr = 1$ case. Crucially, it is the magnitude of the Froude number that is the dominant control of the extremal values of $\Delta\tilde{x}_f^1$ and their locations rather than the ambient depth $\tilde{L}_3$, figures 8, 10 and 11.

3.4. *Depth-resolving model*

Cases 28–33 are run with passive scalars to track the propagation and mixing of material from the two locks, using the methods outlined in § 2.2.2. Plots of the LBM predictions of front location for Cases 28–33 are presented in figure 12. The front location of the instantaneous release, Case 28 where ($\tilde{t}_{re} = 0.0$), is the baseline against which the propagation of the pulsed currents is measured.

The structure of the $\Delta\tilde{x}_f^1$ curves are the same as those observed in the results of physical experiments and LBM simulations for Cases 25–27. At early non-dimensional times the pulsed currents fall behind the instantaneous release current, as they exit the slumping stage of the flow at an earlier time. The distance between the pulsed and instantaneous currents increases until the second pulse merges with the first at $\tilde{t} = \tilde{t}_M$. After merging, the unified front accelerates relative to the single release current. As observed in the deep-ambient experiments, the pulsed currents with relatively short delay times between releases – in this data set $\tilde{t}_{re} \in \{1.5, 2.5, 5.0\}$ – accelerated beyond the single release current, ultimately plateauing with a relative front location of $\Delta\tilde{x}_f^1 > 0$. As observed in the experiments, the relative front locations of the faster currents oscillate around a positive $\Delta\tilde{x}_f^1$ value, which makes it challenging to definitively state which delay time produces the
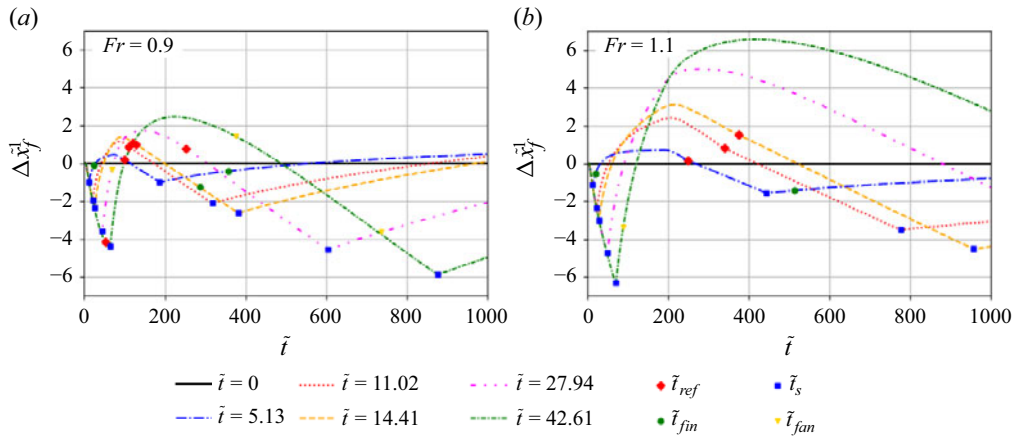
Figure 11. Relative displacement between single and phased releases ($\Delta \tilde{x}_f^1$) for Cases 1–6, which approximate an infinitely deep ambient ($\tilde{L}_3 \to \infty$), for (a) $Fr = 0.9$ and (b) $Fr = 1.1$. The times $t_{ref}(\blacklozenge)$, $t_s(\blacksquare)$ and $t_{fin}(\bullet)$ indicate when the key characteristic curve or the shock intersects the head of the flow. The first occurrence of t_{fan}, t_{ref} and t_{fin} are suppressed for clarity.
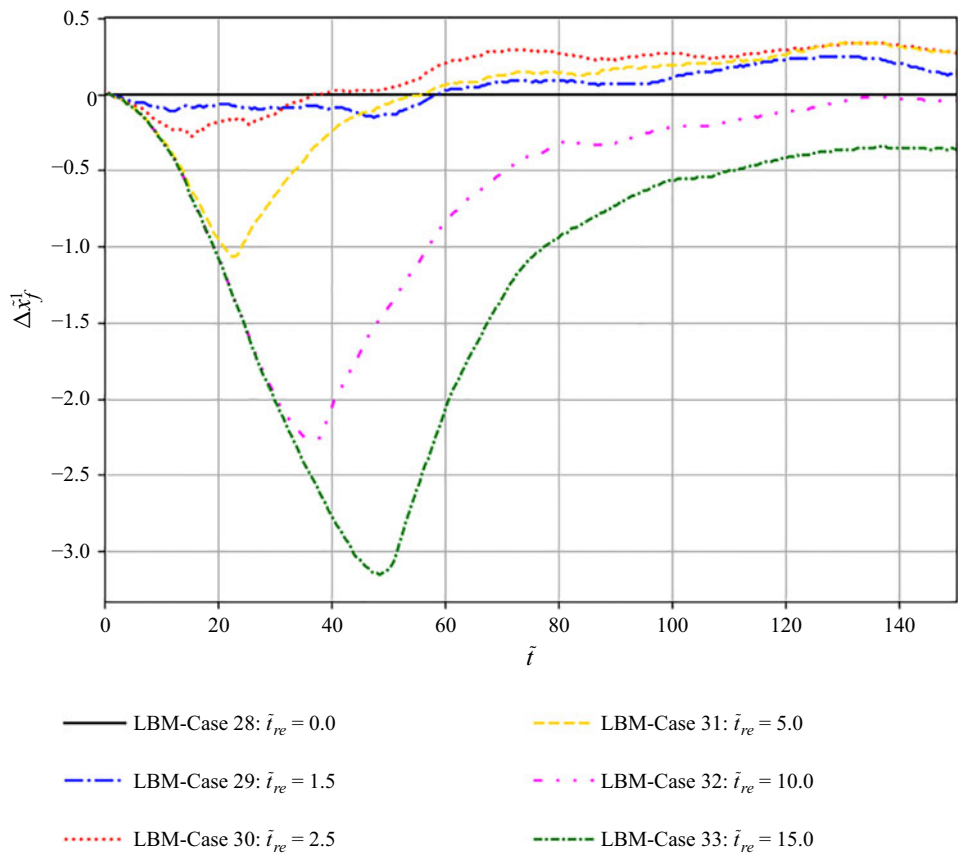

Figure 12. Plots of head location of leading currents relative to the baseline single stage release case ($\Delta \tilde{x}_f^1$) in depth-resolving simulations of Cases 28–33.

fastest current. The relative front location of the pulsed release with $\tilde{t}_{re} = 10$ plateaued at the value $\Delta\tilde{x}_f^1 = 0$, while the $\tilde{t}_{re} = 15$ case plateaued at a value of $\Delta\tilde{x}_f^1 \approx -0.5$.

The results demonstrate that the key result of the physical experiments – short delays between releases generate faster currents than are produced by an instantaneous release of an equal volume of dense material – is robust to changes in the lock aspect ratio.

3.4.1. *Visualisation of dense intrusions using passive scalar fields*

The passive scalar fields $\tilde{\rho}_{P1}$ and $\tilde{\rho}_{P2}$ are used to track dense material released from the first and second lock, respectively. The passive scalar density fields are visualised using RGB contour plots. In the RGB plots pixels are coloured according to fluid concentration, with $\tilde{\rho}_{P1} = 1 \wedge \tilde{\rho}_{P2} = 0$ and $\tilde{\rho}_{P2} = 1 \wedge \tilde{\rho}_{P1} = 0$ corresponding to cyan and purple, respectively. Densities of $\tilde{\rho}_{P1} = 0 \wedge \tilde{\rho}_{P2} = 0$ map to white pixels. A mixture of dense material produces a mix of cyan and purple, providing a qualitative visual measure of pulse mixing.

Plots of spanwise averaged RGB density contours from the depth-resolving simulation of Case 31, $\tilde{t}_{re} = 5.0$, are presented in figure 13. The RGB contours show that the LBM simulations capture the intrusion of the second gravity current into the first. The advancing front of the dense intrusion is highlighted in figure 13(*e*). The leading nose of the second pulse, tracked by the $\tilde{\rho}_{P2}$ density field, is elevated above a layer of dense fluid in the body of the leading current as it propagates at the height of neutral buoyancy. These qualitative features of the flow were impossible to verify when visualising simulations of pulsed currents using a single scalar. Although we do not have validation data for Case 31, we can make qualitative comparisons with physical scale experiments. We observe good qualitative agreement between the elevated nose observed in the LBM results, and the intrusion structure observed in the Ho *et al.* (2018*a*) experiments, presented in figure 1. The RGB contours indicate that the intrusion remains largely separate from the leading gravity current until it arrives at the head and undergoes turbulent mixing. In the following subsections, the mechanics of the intrusion are quantitatively analysed to determine the underlying controls.

3.4.2. *Analysis of the drag forces acting on intrusion boundaries*

The focus of the study now shifts to the objective of understanding the mechanisms that determine whether or not a pulsed current accelerates beyond an instantaneous release current of an equivalent volume of fluid. A secondary objective is to understand why the depth-averaged model does not reproduce this finding, instead predicting that any delay time between releases results in a faster current, and that the maximum observed $\Delta\tilde{x}_f^1$ increases with increasing $\tilde{t}_{re}$. Our working hypothesis is that the relative acceleration of pulsed currents is controlled by the stresses experienced by the dense intrusion as it propagates to the head. The stresses acting on the dense intrusion prior to the merge time $(\tilde{t}_M)$ for Cases 28–33 are quantitatively analysed using the results of the LBM simulations.

Prior to $\tilde{t}_M$ the pulsed current can be conceptualised as a dense intrusion propagating through a moving ambient. The interface between the currents is identified through the passive scalar density fields, denoted $\tilde{\rho}_{P1}$ and $\tilde{\rho}_{P2}$, which track material released from the first and second lock, respectively. The boundary between the dense intrusion and surrounding fluid is defined as the isoline $\boldsymbol{I}(\tilde{t})$. To define $\boldsymbol{I}(\tilde{t})$ we need to assign a density value for the current–ambient interface. Here we set the nominal density threshold to $\tilde{\rho}_{P2}^* = 0.02$, motivated by the empirically validated use of this value by Ottolenghi *et al.* (2016, 2018) to model mixing and entrainment in gravity currents. The isolines for the intrusion boundaries in the LBM simulation of Case 31 are plotted in figure 14.
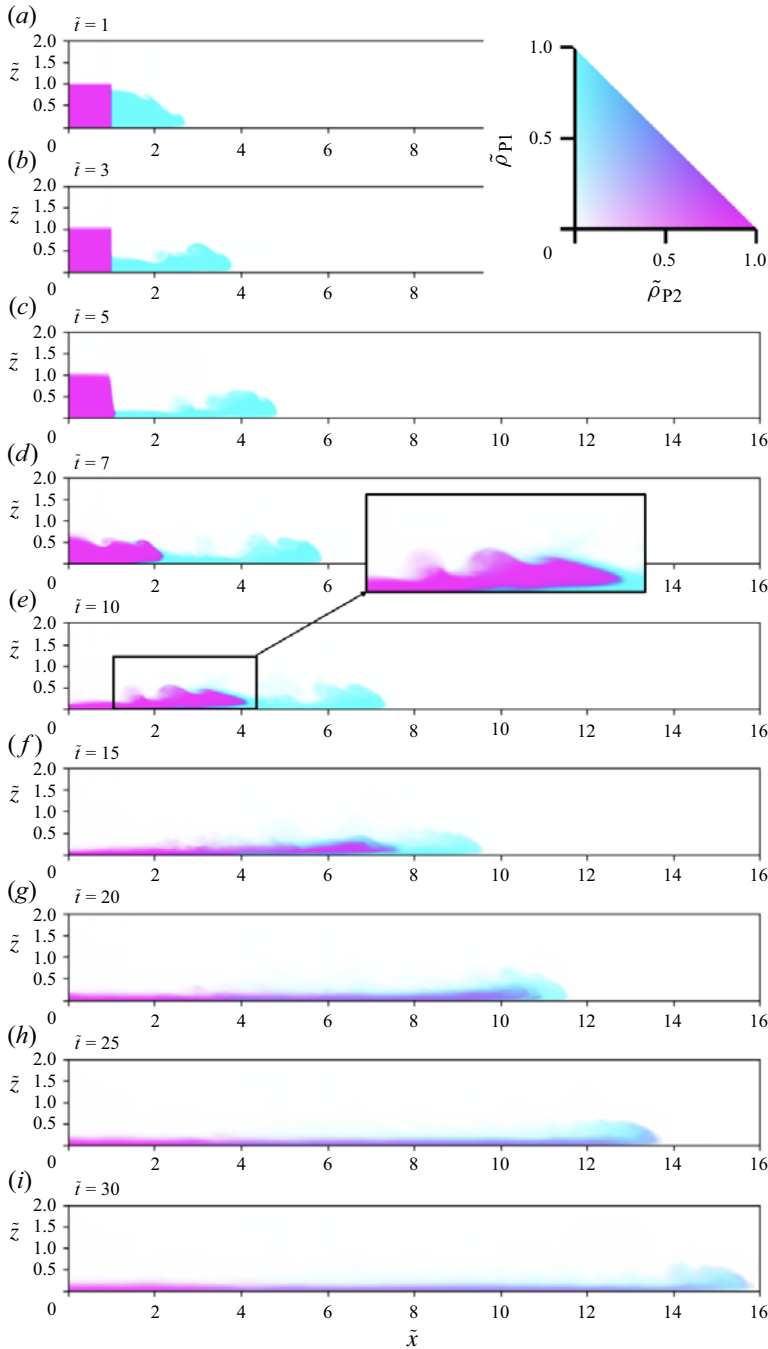
Figure 13. Red–green–blue (RGB) contour plot of density in the LBM pulsed gravity current simulation of Case 31, $\tilde{t}_{re} = 5$. Passive scalars are used to track the propagation and mixing of dense material from each lock. The density field $\tilde{\rho}_{P1}$ tracks material from the first lock, while the field $\tilde{\rho}_{P2}$ tracks material from the second lock. Pixels are coloured according to fluid concentration, with $\tilde{\rho}_{P1} = 1 \wedge \tilde{\rho}_{P2} = 0$ and $\tilde{\rho}_{P2} = 1 \wedge \tilde{\rho}_{P1} = 0$ corresponding to cyan and purple, respectively. Densities of $\tilde{\rho}_{P1} = 0 \wedge \tilde{\rho}_{P2} = 0$ map to white pixels. A mixture of dense material produces a mix of cyan and purple, as indicated by the colour scale. Contours are plotted at times (*a*) $\tilde{t} = 1$, (*b*) $\tilde{t} = 3$, (*c*) $\tilde{t} = 5$, (*d*) $\tilde{t} = 7$, (*e*) $\tilde{t} = 10$, (*f*) $\tilde{t} = 15$, (*g*) $\tilde{t} = 20$, (*h*) $\tilde{t} = 25$, (*i*) $\tilde{t} = 30$.

Figure 14. Plots of the density isolines that define the boundary of the leading pulse and the dense intrusion triggered by the release of the second lock gate in the LBM simulations of Case 31, $\tilde{t}_{re} = 5$. The current–ambient interface is defined as the longest continuous isoline of the density threshold $\tilde{\rho}_{P1}^* = 0.02$ for the leading current (solid line), and $\tilde{\rho}_{P2}^* = 0.02$ for the dense intrusion (dashed line).

Case	$\tilde{t}_{re}$	$\tilde{t}_M$	$\tilde{L}_M$
28	0.00	8.00	6.34
29	1.50	9.00	6.82
30	2.50	11.00	7.74
31	5.00	19.50	11.18
32	10.00	33.5	15.37
33	15.00	45.5	18.05

Table 2. Results for pulse merge time $\tilde{t}_M$ and the location of the intrusion front at the time of pulse merging $\tilde{L}_M$ in the LBM simulations of Cases 28–33, which have dual-stage release delay times $\tilde{t}_{re} \in [0.00, 15.00]$. The pulses are said to have merged when the distance between their respective fronts is less than or equal to $\tilde{x}_0$.

These isolines are extracted by applying the $\tilde{\rho}_{P2}^* = 0.02$ threshold to the $\tilde{\rho}_{P2}$ field in the RGB contour plots in figure 13.

The non-dimensional drag coefficient (C_D) is an analytical tool for quantifying the resistance experienced by a flow. Here we apply the concept to the dense intrusion prior to merging with the leading current, defining the drag coefficient as the dimensionless measure of resistance due to the sum of skin friction drag (C_f) and form drag. The drag force (F_D) is the force acting in the opposite direction to the predominant flow velocity u. The skin-friction coefficient is a non-dimensional measure of resistance due to friction at an interface (Tritton 2012). In turbulent gravity currents the skin-fiction coefficient, due to shear at the lower boundary of the body, is of the order 10^{-3} (Wells & Dorrell 2021). This is true at both the laboratory and environmental scale.

As the shape and volume of the dense intrusion change continuously between the release of the current and the merge time, it is necessary to normalise the absolute stresses acting on the intrusion by the length of the boundary of the intrusion $L_{I,B}$. This length is the sum of the length of the isoline $\boldsymbol{I}(\tilde{t})$, and the curve that defines the contact line between the boundary walls and the current $\boldsymbol{B}(\tilde{t})$. Additionally, the values used to calculate the drag coefficients are averaged over the time between the release of the current at $\tilde{t} = \tilde{t}_{re}$ and the merge time $\tilde{t} = \tilde{t}_M$. The merge time ($\tilde{t}_M$) and current front location at the time of merging ($\tilde{L}_M$) for Cases 28–33 are presented in table 2. The pulses are said to have merged when the intrusion produced by the second release has entered the head of the leading current. We make the conservative estimation that the intrusion has entered the head of the leading current when the distance between their respective fronts is less than or equal to $\tilde{x}_0$.

In order to calculate the skin-friction and drag coefficients for the dense intrusions it is necessary to calculate the cumulative skin-friction force (F_f) and drag force (F_D) acting on the boundary of the intrusion. This is achieved by computing the line integral of the fluid shear stresses along the current–ambient interface isoline $\boldsymbol{I}(\tilde{t})$, and the curve that defines the contact line between the boundary walls and the current $\boldsymbol{B}(\tilde{t})$. This is in effect the dashed closed curve that bounds the intrusion in figure 14. The shear stress field is spanwise averaged, resulting in a 2-rank tensor $\tilde{\tau}(\tilde{x}, \tilde{z}, \tilde{t})$ that defines the shear stress in the field. The shear stresses are calculated from the velocity field $\tilde{\boldsymbol{u}}(\tilde{\boldsymbol{x}}, \tilde{t})$ predicted by the LBM model run in VirtualFluids.

The total skin-friction force acting on the boundary of the intrusion is calculated as the line integral along the curves $\boldsymbol{I}(\tilde{t})$ and $\boldsymbol{B}(\tilde{t})$ of the stress acting tangential to the intrusion boundary $\tilde{\tau}_s$, i.e. the skin-friction shear stress,

$$F_f(\tilde{t}) = \int_{C=\boldsymbol{I}\cup\boldsymbol{B}} \tilde{\tau}_s(\tilde{\boldsymbol{x}}, \tilde{t})\, \mathrm{d}C. \tag{3.5}$$

1026 A14-27

The total drag force acting on the boundary of an intrusion $F_D(\tilde{t})$ as a function of time $\tilde{t}$, is calculated by integrating the stress acting in the opposite direction to the velocity of the intrusion front ($\tilde{\tau}_{xz}(\tilde{\boldsymbol{x}}, \tilde{t})$) along the curves $\boldsymbol{I}(\tilde{t})$ and $\boldsymbol{B}(\tilde{t})$,

$$F_D(\tilde{t}) = \int\limits_{C=\boldsymbol{I}\cup\boldsymbol{B}} \tilde{\tau}_{xz}\left(\tilde{\boldsymbol{x}}, \tilde{t}\right) \, \mathrm{d}C. \tag{3.6}$$

The stresses experienced by the intrusion are dynamic. To compute coefficients for the lifetime of the intrusion, i.e. from its release at $\tilde{t}_{re}$ to the merge time $\tilde{t}_M$, the resistive forces are averaged over the time period $[\tilde{t}_{re}, \tilde{t}_M]$. The equation

$$
\begin{aligned}
C_f &= \frac{2}{\tilde{\rho}} u^{-2} \tau_f \\
&= \frac{2}{\tilde{\rho}} \left(\frac{\tilde{L}_M}{\tilde{t}_M - \tilde{t}_{re}}\right)^{-2} \frac{1}{\tilde{t}_M - \tilde{t}_{re}} \int\limits_{\tilde{t}_{re}}^{\tilde{t}_M} \frac{F_f(\tilde{t})}{L_{\boldsymbol{I},\boldsymbol{B}}(\tilde{t})} \, \mathrm{d}\tilde{t}
\end{aligned} \tag{3.7}
$$

is used to calculate a skin-friction coefficient for an intrusion. The velocity is taken to be the average speed of the intrusion front prior to $\tilde{t}_M$, i.e. $u = \tilde{L}_M/(\tilde{t}_M - \tilde{t}_{re})$. The average skin-friction stress τ_f is defined as the time average of the spatially averaged skin-friction stress acting on the boundary intrusion as a function of time, $F_f(\tilde{t})/L_{\boldsymbol{I},\boldsymbol{B}}(\tilde{t})$. The equation

$$
\begin{aligned}
C_D &= \frac{2}{\tilde{\rho}} u^{-2} \tau_D \\
&= \frac{2}{\tilde{\rho}} \left(\frac{\tilde{L}_M}{\tilde{t}_M - \tilde{t}_{re}}\right)^{-2} \frac{1}{\tilde{t}_M - \tilde{t}_{re}} \int\limits_{\tilde{t}_{re}}^{\tilde{t}_M} \frac{F_D(\tilde{t})}{L_{\boldsymbol{I},\boldsymbol{B}}(\tilde{t})} \, \mathrm{d}\tilde{t}
\end{aligned} \tag{3.8}
$$

is used to calculate a drag coefficient for an intrusion. The average drag stress τ_D is defined as the time average of the spatially averaged total drag stress acting on the boundary intrusion as a function of time $F_D(\tilde{t})/L_{\boldsymbol{I},\boldsymbol{B}}(\tilde{t})$.

The skin-friction (C_f) and drag coefficients (C_D) of dense intrusions in the LBM simulations of Cases 28–33 are presented in table 3. Alongside the absolute values, the ratio between the coefficients for each delay time and the respective coefficient for the $\tilde{t}_{re} = 0$ instantaneous release case is also tabulated. The results for the skin-friction and drag coefficients are all of the order of magnitude 10^{-3}, which provides confidence in the method used, as this is the same order of magnitude that has been documented in the literature for the skin friction in the body of a gravity current (Wells & Dorrell 2021).

The ratio between the skin-friction coefficient for the pulsed intrusions and the instantaneous release intrusions shows that the delay times that produced faster currents, $\tilde{t}_{re} \in \{1.50, 2.50, 5.00\}$ had intrusions that experienced the least resistance due to skin-friction prior to the merge time $\tilde{t}_M$. However, the two cases that did not result in slower currents $\tilde{t}_{re} \in \{10.00, 15.00\}$, also experience less skin-friction resistance than the single release case intrusion. Therefore, lower skin-friction prior to $\tilde{t}_M$ is not entirely predictive of a faster current postmerging. The computed drag coefficients are larger than the skin-friction coefficients, which is expected as C_D includes the additional effect of form drag, i.e. drag due to the intrusion's shape. The ratio between the drag coefficient for the pulsed intrusions and the instantaneous release intrusions shows that the delay times that produced faster currents had intrusions that experienced less drag than the $\tilde{t}_{re} = 0$ case

Case	$\tilde{t}_{re}$	Faster or slower	C_f	$C_f/C_f^{\tilde{t}_{re}=0}$	C_D	$C_D/C_D^{\tilde{t}_{re}=0}$
28	0.00	$\sim$	0.0030	1.00	0.0033	1.00
29	1.50	F	0.0020	0.65	0.0022	0.67
30	2.50	F	0.0020	0.66	0.0021	0.65
31	5.00	F	0.0023	0.77	0.0027	0.83
32	10.00	$\sim$	0.0024	0.79	0.0031	0.96
33	15.00	S	0.0028	0.92	0.0037	1.13

Table 3. Results for the skin-friction coefficient (C_f) and the drag coefficient (C_D) of the dense intrusion in the LBM simulations of the pulsed gravity currents in Cases 28–33. The drag coefficients are time averaged between the release of the current at $\tilde{t} = \tilde{t}_{re}$ and the merge time $\tilde{t} = \tilde{t}_M$. The pulses are said to have merged when the intrusion has entered the head of the leading current, i.e. when the distance between their respective fronts is less than or equal to $\tilde{x}_0$. The ratio between the coefficients for the instantaneous release, Case 28, and each pulsed release are also tabulated in the $C_f/C_f^{\tilde{t}_{re}=0}$ and the $C_D/C_D^{\Delta\tilde{t}_{re}=0}$ columns. Additionally, whether or not the delay time resulted in a pulse that was faster (F), slower (S) or of equal speed ($\sim$) after $\tilde{t}_M$ is also documented.

prior to the merge time. However, the drag coefficient ratio for the intrusion in Case 32 is $C_D/C_D^{\tilde{t}_{re}=0} = 0.96$, indicating the intrusion experienced approximately equal (within 4 %) drag resistance to the intrusion in the instantaneous release simulation. A review of the relative front location curve ($\Delta\tilde{x}_f^1$), see figure 12, shows that postmerging the relative front location plateaued approximately equal to the single release case.

The drag coefficient ratio for the intrusion in Case 33 is $C_D/C_D^{\tilde{t}_{re}=0} = 1.13$, meaning the intrusion experienced 13 % more drag than the instantaneous release intrusion. The plots of relative front location (figure 12) show that this case resulted in a slower current after the merge time. The results demonstrate that the time averaged drag coefficient of the intrusion prior to $\tilde{t}_M$ is predictive of the speed of the current postmerging relative to an instantaneous release current. Interestingly, the skin-friction coefficients do not capture this trend. This provides evidence that it is an increase in relative form drag on the intrusion for larger $\tilde{t}_{re}$ that results in a slower current. A reduction in drag means that short delays between releases result in dense intrusions that dissipate less energy relative to an instantaneous release prior to $\tilde{t}_M$, and therefore supply more energy to the head of the leading current when they merge. Long delays between releases result in intrusions that deliver less energy to the leading current at $\tilde{t}_M$, relative to an instantaneous release.

The drag analysis results are potentially sensitive to the assigned nominal density of the current–ambient interface, $\tilde{\rho}_{P2}^* = 0.02$. Therefore, to assess the sensitivity of C_f and C_D to variation in the interface density. We set the current–ambient interface threshold to six values spread logarithmically over two orders of magnitude; $\tilde{\rho}_{P2}^* \in [0.001, 0.1]$. For each $\tilde{\rho}_{P2}^*$ value we calculate C_f and C_D for $\tilde{t}_{re} \in \{1.50, 2.50, 5.00, 10.00, 15.00\}$. The results are presented in figure 15, where we plot the coefficients relative to their respective values in the case $\tilde{t}_{re} = 0$, that is, $C_f/C_f^{\tilde{t}_{re}=0}$ and $C_D/C_D^{\tilde{t}_{re}=0}$. The solid curves in figure 15 are the median values of the coefficients, while the shaded region represents the interval P2.5 to P97.5. The results show that although uncertainty in $\tilde{\rho}_{P2}^*$ propagates through to a spread in computed C_f and C_D, the trends in the results are unchanged. We find that currents with delay times of $\tilde{t}_{re} \in \{1.50, 2.50, 5.00\}$ experience the smallest skin-friction and drag coefficients, and that all release times result in $C_f/C_f^{\tilde{t}_{re}=0} < 1$. Critically, whilst accounting for uncertainty in $\tilde{\rho}_{P2}^*$, we still observe that Case 33 – the intrusion generated by the longest delay time between releases ($\tilde{t}_{re} = 15.00$) – is the only one to experience a drag
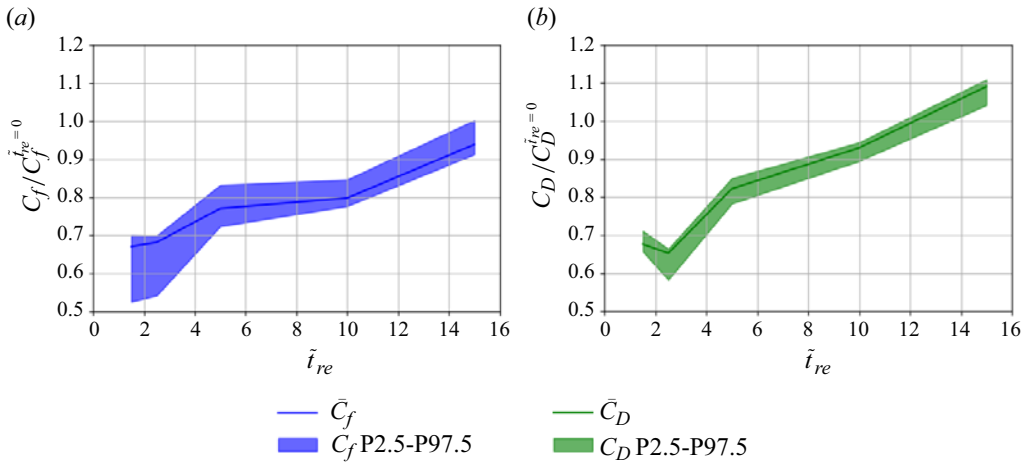
(*a*)   (*b*)

Figure 15. Sensitivity analysis results for the skin-friction coefficient C_f and the drag coefficient C_D of the dense intrusion in the LBM simulations of the pulsed gravity currents. We vary the current–ambient interface density threshold logarithmically across the range $\tilde{\rho}_{P2}^* \in [0.001, 0.1]$. For each $\tilde{\rho}_{P2}^*$ value we calculate C_f and C_D for $\tilde{t}_{re} \in \{1.50, 2.50, 5.00, 10.00, 15.00\}$. Here $C_f/C_f^{\tilde{t}_{re}=0}$ and $C_D/C_D^{\tilde{t}_{re}=0}$ are the coefficients relative to their respective values at $\tilde{t}_{re} = 0$.

resistance greater than an equivalent instantaneous release. This reinforces the finding that the time averaged drag coefficient of the intrusion prior to $\tilde{t}_M$ is predictive of current speed postmerging, and demonstrates that the result is robust to uncertainty in $\tilde{\rho}_{P2}^*$, within the ranges considered.

4. Discussion

The present study uses experiments, depth-averaged simulations and depth-resolving models to study the dynamics of pulsed gravity currents. Analysis of the experimental results reveals a new and important finding; that pulsed gravity currents with short delay times between releases can propagate faster than an instantaneous release of an equal volume of dense material, after the two pulses have merged. However, it was found that longer delays between releases resulted in slower currents. Given a fractional depth of release of $h_0/L_3 = 0.2$, physical experiments show that delay times of $\tilde{t}_{re} \in \{5.13, 11.02\}$ result in faster currents postmerging, while delay times of $\tilde{t}_{re} \in \{14.41, 27.94, 42.61\}$ produced slower currents. The experimental results for $h_0/L_3 = 0.5$, show that a delay time of $\tilde{t}_{re} = 5.14$ produces a faster current, while $\tilde{t}_{re} = 10.15$ generates a slower current. This result has implications for our understanding of environmental gravity currents. Pulsed currents arise naturally due to a range of causes including successive slope failures on the continental shelf, intermittent seismic activity and the merging of currents at channel confluences (Goldfinger *et al.* 2017). Additionally, their dynamics have implications for the geohazard risks posed by pyroclastic flows, avalanches and turbidity currents (Loughlin *et al.* 2002). The key research objectives are to understand the mechanisms that produce the observed phenomena and assess the ability of conventional geohazard prediction models to capture the dynamics of the pulsed currents.

Depth-averaged simulations predict a different trend to that observed in the physical experiments; pulsed currents are found to always generate faster flows after the pulses merged, and increasing delays between releases resulted in increasingly faster currents after merging. There is an overlap between the parameters used to generate the

experimental, depth-averaged and depth-resolving LBM data sets, allowing for direct comparison between the predictions of each method. The LBM model reproduces the same findings observed in the experimental results, and shows close agreement in the prediction of front location across a range of delay times. The depth-averaged simulations show close agreement with the experiments and depth-resolving simulations at early times, but diverge when the flow enters the viscous phase, as the shallow-water equations neglect viscous terms in the governing equations.

The depth-resolving models permit more detailed analysis of the flow using passive scalars to track the propagation, mixing and merging of material from each lock. Here the level of resistance experienced by the intrusion prior to merging was shown to be predictive of the speed relative to an instantaneous release current. This was demonstrated by computing the skin-friction and drag coefficients of the intrusions. The results confirmed that intrusions generated by pulsed currents with short delays between releases experienced less skin-friction and total drag resistance prior to merging than instantaneous release intrusions. Long delays between releases resulted in intrusions with lower skin-friction resistance than an instantaneous release intrusion, but critically higher total drag resistance. A sensitivity analysis showed that the trends were robust to uncertainty in the current–ambient interface density. This result demonstrates that a delay between releases reduces the skin-friction resistance experienced by an intrusion, likely due to the propagation of the second current over the layer of dense material deposited by the first release. It should be noted that as the delay time increases, this effect diminishes, as can be seen in the skin-friction coefficient results. However, it is an increase in form drag acting on intrusions with longer delay times that is responsible for the slower propagation of these currents. This partially explains the inability of depth-averaging simulations to capture this phenomenon, as they do not resolve the detailed shape of the intrusion front, instead modelling it as a sharp discontinuity regardless of delay time. Therefore, such models are not able to capture the increase in form drag that results from the intrusion being less sheltered by the residual density field of the first current. In environmental settings the faster flows created by pulsed gravity currents may more readily suspend and entrain sediment, in turn extending run out distances. Real world flows will also be complicated by differing volumes and densities of sequential release, slopes and topography interactions. Moreover, naturally occurring gravity currents typically flow on a downward slope and may be unstable to roll-waves, which can give rise to internal pulses that propagate faster than the front. These may all act to enhance (or diminish) the generation of intrusions within gravity currents.

The physical experiments and LBM simulations are limited by physical scale and computational expense, respectively, preventing them from reaching the high buoyancy Reynolds numbers that would generate a highly turbulent flow throughout the experimental run time. Therefore, care must be taken when extrapolating to highly turbulent environmental scale flows. In the present study all simulations were run for a buoyancy Reynolds number of $Re_b \approx 6000$. The effect of Reynolds number on the results could be the subject of further research.

The depth-averaged simulations model the second release as a propagating shock with uniform flow properties throughout the current depth. This is fundamentally different to the drag reducing intrusions observed in the physical experiments and LBM simulations. It has been demonstrated that density stratification models are critical for the modelling of gravity current run-out (Dorrell *et al.* 2014; Wells & Dorrell 2021). Additionally, the SWE model does not currently include entrainment. The three-equation entrainment model has been used in combination with an infinite depth ambient to study the impact of entrainment on front propagation (Johnson & Hogg 2013). However, extending the finite

depth shallow-water equations to include entrainment has, to the authors' knowledge, not been demonstrated before. Such model extensions were outside the scope of the present study.

Incorporating density stratification and entrainment in finite-depth SWE models of pulsed currents may help to address the existing limitations of the depth-averaged simulations and should be considered in future research.

5. Conclusion

A comparison of methods to predict and understand the dynamics of pulsed gravity currents was made. Physical scale experiments were used to quantify front propagation rates and merging times between sequential releases. Further, a depth-averaged shallow water model and a full three-dimensional LBM simulation were developed to investigate the dynamics observed in the physical experiments. The study covers a broad parameter space including a wide range of delay times between releases, fractional depths of release and lock aspect ratios.

Crucially it is shown, for the first time, that pulsed gravity currents with short delay times between releases propagate faster than an instantaneous release of an equal volume of dense material, while longer delays result in slower currents. The results from the physical experiments and LBM modelling highlight the critical role of intrusions, enabled by vertical variation in flow density, in the dynamics of pulsed flow propagation.

Intrusions in pulsed flows that propagate faster than instantaneous releases are shown to experience less drag resistance, and therefore dissipate less energy. Depth-averaged simulations were unable to capture this phenomenon as they do not resolve the intrusion shape, and so cannot effectively predict form drag. Further research is required to understand the trigger mechanisms of natural hazards, including pulsed events, to better enable the prediction and mitigation of their risks.

Declaration of interests. The authors report no conflict of interest. The funders had no role in study design, the collection, analysis and interpretation of data, or in the preparation of the article and decision to publish.

Appendix A. Shallow-water numerical solver and verification

The shallow-water equations with the initial and boundary conditions reflecting a double-lock release problem are solved using a Lax–Wendroff finite-difference scheme. For more details see the appendix of Bonnecaze *et al.* (1993) and Allen *et al.* (2020). When solving the shallow-water equations, the second lock box is neglected when $t < t_{re}$, and the coordinates are translated so that the left-hand boundary of the flow (front of the second lock box) is at $x = 0$. The equations are scaled using the following coordinate transform $(\zeta, \tau) = (x/x_f^1(t), t)$:

$$\frac{\partial h}{\partial t} = \frac{1}{x_f^1} \left(\dot{x}_f^1 \zeta \frac{\partial h}{\partial \zeta} - \frac{\partial m}{\partial \zeta} \right), \tag{A1}$$

$$\frac{\partial m}{\partial t} = \frac{1}{x_f^1} \left[\left(\zeta \dot{x}_f^1 - \frac{m}{h}(2 - 2a) \right) \frac{\partial m}{\partial \zeta} + \left(\frac{m^2}{h^2}(1 - 2a) - h(1 - b) \right) \frac{\partial h}{\partial \zeta} \right], \qquad (A2)$$

where t is replaced with τ for convenience and a and b remain unchanged. In characteristic form the two-layer shallow-water ((A1) and (A2)) are

$$\frac{\mathrm{d}h}{\mathrm{d}u} = \frac{1}{1-b} \left(au \mp \sqrt{a^2 u^2 + (1-b)h} \right) \qquad (A3)$$

on

$$\frac{\mathrm{d}\zeta}{\mathrm{d}t} = \frac{1}{x_f^1} \left[u(1-a) - \zeta \dot{x}_N \pm \sqrt{a^2 u^2 - (1-b)h} \right] = c_{\pm}. \qquad (A4)$$

In the deep ambient limit $\tilde{L}_3 \to \infty$, these reduce to the characteristic curves for the single-layer SWEs and can be integrated to obtain the Riemann invariants of the single-layer shallow-water equations (Stoker 2011). In practice the reduced deep ambient limit equations could be solved as a separate case as in Allen *et al.* (2020). However, a suitably large value of $\tilde{L}_3 = 10^4$ is chosen instead. Increasing or decreasing this value by an order of magnitude does not change the solutions. In a deep ambient case the values $\alpha = u + 2\sqrt{h}$ and $\beta = u - 2\sqrt{h}$ are conserved along positive or negative characteristics, respectively. To correctly impose the front boundary condition $u_f^1 = Fr(h_f^1/)\sqrt{h_f^1}$ the positive characteristic arriving at the head at the next time step needs to be determined. This provides the second condition on for h_f^1 and u_f^1 at the head of the flow. The method is similar to Ungarish & Zemach (2005), who instead integrate forward from the unperturbed region of the flow.

A grid resolution of $\Delta\zeta = 0.001$ is used to discretise the scaled domain into $N_x = 1001$ equally spaced grid points. At $t = \tilde{t}_{re}$, $\lfloor Nx/N_x \rfloor$ additional nodes are included to represent the fluid in the second lock box, where $\lfloor \ \rfloor$ is the floor function. This changes the unit interval to $[-1/x_f^1(\tilde{t}_{re}, 1)]$, which is then rescaled back to the unit interval [0,1]. This ensures the same number of nodes remain in the body of the first release and removes the need to interpolate the solution at $t = \tilde{t}_{re}$. Time stepping is controlled by a Courant number condition

$$\delta t = Cr \frac{\min_i \Delta x_i}{\max_i (|c_{+i}|, |c_{-i}|)}, \qquad (A5)$$

where $c_{\pm i}$ are the wave speeds at node i. A necessary but not sufficient condition for stability in a numerical scheme is $Cr < 1$. A conservative value of $Cr = 0.1$ was chosen as a balance between numerical stability and computational cost. This gives an added advantage that, provided there is rapid changes in the solution at the head, the positive characteristic that arrives at the head at the next time step originates between the last two grid nodes. By using this Courant condition based on the wave speeds it is guaranteed that the positive characteristic arriving at the head of the flow at the next time step originates in between the last two nodes of the domain. The average values between the last two cells $(h_{N-1/2}^n, u_{N-1/2}^n)$ are used as initial conditions when first solving for the head height and velocity at the next time step (h_N^{n+1}, u_N^{n+1}),

$$\frac{\mathrm{d}h}{\mathrm{d}u} = \frac{1}{1-b} \left(au - \sqrt{a^2 u^2 + (1-b)h} \right). \qquad (A6)$$

The characteristic gradient (A4) is then backwards integrated in time using a first-order upwind method to obtain a more accurate starting location for the characteristic arriving

at the head $\zeta = \zeta_s$. Using linear interpolation between the final two nodes, the depth h_{ζ_s} and u_{ζ_s} velocity at the point $\zeta = \zeta_s$ is obtained and used as initial conditions to solve equation (A6) again to obtain a more accurate estimate of the head depth and velocity (h_N^{n+1}, u_N^{n+1}). After investigation, repeating the process to find further better estimates made no difference to the obtained solutions.

A small artificial viscosity term $\sim b_1 \partial^2 u / \partial \zeta^2$, the same form as used by Ungarish & Zemach (2005) and similar to Bonnecaze *et al.* (1993) and Allen *et al.* (2020) was introduced to dampen spurious oscillations that appear within the solution that can lead to divergence if allowed to grow over time. These arises behind the head and the shock during the first few time steps after the first and second release. A coefficient $b_1 = 1$ removes the vast majority of these oscillations. The exception is for the longest release times, where small oscillations can be observed behind the shock until it reaches the head of the flow. These dissipate after the shock reflects backwards after reaching the head. At $T = 100$, which is sufficient time for the shock to reach the head in all release times t_{re} presented in this paper, the diffusion coefficient is reduced to $b_1 = 0.1$. Keeping the diffusion coefficient at $b_1 = 1$ led to numerical instability as the current became very thin and further, this additional diffusion is only necessary during the early stages when the jumps at the shock are large.

REFERENCES

ADEKANYE, D., KHAN, A., BURNS, A., MCCAFFREY, W., GEIER, M., SCHÖNHERR, M. & DORRELL, R. 2022 Graphics processing unit accelerated lbm simulations of dilute gravity currents. *Phys. Fluids.* **34**, 046602.

ALLEN, P.A. 2018 *Pulse Propagation in Quasi Laminar Gravity Currents - Dataset*. University of Leeds.

ALLEN, P.A., DORRELL, R.M., HARLEN, O.G., THOMAS, R.E. & MCCAFFREY, W.D. 2020 Pulse propagation in gravity currents. *Phys. Fluids* **32** (1), 016603.

ANDREWS, B.J. & MANGA, M. 2012 Experimental study of turbulence, sedimentation, and coignimbrite mass partitioning in dilute pyroclastic density currents. *J. Volcanol. Geoth. Res.* **225–226**, 30–44.

BEESON, J.W., JOHNSON, S.Y. & GOLDFINGER, C. 2017 The transtensional offshore portion of the northern San Andreas fault: fault zone geometry, late Pleistocene to Holocene sediment deposition, shallow deformation patterns, and asymmetric basin growth. *Geosphere* **13** (4), 1173–1206.

BENJAMIN, T.B. 1968 Gravity currents and related phenomena. *J. Fluid Mech.* **31** (2), 209–248.

BONNECAZE, R.T., HUPPERT, H.E. & LISTER, J.R. 1993 Particle-driven gravity currents. *J. Fluid Mech.* **250**, 339–369.

BONOMETTI, T. & BALACHANDAR, S. 2008 Effect of Schmidt number on the structure and propagation of density currents. *Theor. Comp. Fluid Dyn.* **22** (5), 341.

CANTERO, M.I., LEE, J.R., BALACHANDAR, S. & GARCIA, M.H. 2007 On the front velocity of gravity currents. *J. Fluid Mech.* **586**, 1–39.

DAI, A. 2017 Experiments on two-layer density-stratified inertial gravity currents. *Phys. Rev. Fluids* **2** (7), 073802.

DORRELL, R.M., DARBY, S.E., PEAKALL, J., SUMNER, E.J., PARSONS, D.R. & WYNN, R.B. 2014 The critical role of stratification in submarine channels: implications for channelization and long runout of flows. *J. Geophys. Res.: Oceans* **119** (4), 2620–2641.

DUBOIS, F. 2008 Equivalent partial differential equations of a lattice boltzmann scheme. *Comput. Math. Appl.* **55** (7), 1441–1449.

FAY, J.A. 1971 Physical processes in the spread of oil on a water surface. *Intern. Oil Spill Confer. Proc.* **1**, 463–467.

FUKUDA, S. *et al.* 2023 Inadequacy of fluvial energetics for describing gravity current autosuspension. *Nat. Commun.* **14** (1), 2288.

GEIER, M., PASQUALI, A. & SCHÖNHERR, M. 2017 Parametrization of the cumulant lattice boltzmann method for fourth order accurate diffusion part i: derivation and validation. *J. Comput. Phys.* **348**, 862–888.

GEIER, M., SCHÖNHERR, M., PASQUALI, A. & KRAFCZYK, M. 2015 The cumulant lattice boltzmann equation in three dimensions: theory and validation. *Comput. Math. Appl.* **70** (4), 507–547.

GOLDFINGER, C., GALER, S., BEESON, J., HAMILTON, T., BLACK, B., ROMSOS, C., PATTON, J., NELSON, C.H., HAUSMANN, R. & MOREY, A. 2017 The importance of site selection, sediment supply, and

hydrodynamics: a case study of submarine paleoseismology on the Northern Cascadia margin, Washington USA. *Mar. Geol.* **384**, 4–46.

HO, V.L., DORRELL, R.M., KEEVIL, G.M., BURNS, A.D. & MCCAFFREY, W.D. 2018*a* Pulse propagation in turbidity currents. *Sedimentology* **65** (2), 620–637.

HO, V.L., DORRELL, R.M., KEEVIL, G.M., BURNS, A.D. & MCCAFFREY, W.D. 2018*b* Scaling analysis of multipulsed turbidity current evolution with application to turbidite interpretation. *J. Geophys. Res.: Oceans* **123** (5), 3668–3684.

HO, V.L., DORRELL, R.M., KEEVIL, G.M., THOMAS, R.E., BURNS, A.D., BAAS, J.H. & MCCAFFREY, W.D. 2019 Dynamics and deposition of sediment-bearing multi-pulsed flows and geological implication. *J. Sediment. Res.* **89** (11), 1127–1139.

HOGG, A.J. 2006 Lock-release gravity currents and dam-break flows. *J. Fluid Mech.* **569**, 61–87.

HOGG, A.J. & PRITCHARD, D. 2004 The effects of hydraulic resistance on dam-break and other shallow inertial flows. *J. Fluid Mech.* **501**, 179–212.

HOGG, A.J., UNGARISH, M. & HUPPERT, H.E. 2000 Particle-driven gravity currents: asymptotic and box model solutions. *Eur. J. Mechan.-B/Fluids* **19** (1), 139–165.

HOPFINGER, E.J. 1983 Snow avalanche motion and related phenomena. *Annu. Rev. Fluid Mech.* **15** (1), 47–76.

HOULT, D.P. 1972 Oil spreading on the sea. *Annu. Rev. Fluid Mech.* **4** (1), 341–368.

HUPPERT, H.E. 1982 The propagation of two-dimensional and axisymmetric viscous gravity currents over a rigid horizontal surface. *J. Fluid Mech.* **121**, 43–58.

HUPPERT, H.E. 2006 Gravity currents: a personal perspective. *J. Fluid Mech.* **554**, 299–322.

HUPPERT, H.E. & SIMPSON, J.E. 1980 The slumping of gravity currents. *J. Fluid Mech.* **99** (04), 785–799.

JOHNSON, C.G. & HOGG, A.J. 2013 Entraining gravity currents. *J. Fluid Mech.* **731**, 477–508.

JOHNSON, H.P., GOMBERG, J.S., HAUTALA, S.L. & SALMI, M.S. 2017 Sediment gravity flows triggered by remotely generated earthquake waves. *J. Geophys. Res.: Solid Earth* **122** (6), 4584–4600, arXiv:https://agupubs.onlinelibrary.wiley.com/doi/pdf/10.1002/2016JB013689

JONES, T.J., BECKETT, F., BERNARD, B., BREARD, E.C.P., DIOGUARDI, F., DUFEK, J., ENGWELL, S. & EYCHENNE, J. 2023 Physical properties of pyroclastic density currents: relevance, challenges and future directions. *Front. Earth Sci.* **11**, 1218645.

JUNK, M., KLAR, A. & LUO, L.S. 2004 Theory of the lattice boltzmann method: mathematical analysis of the lattice boltzmann equation, preprint.

KLEMP, J.B., ROTUNNO, R. & SKAMAROCK, W.C. 1994 On the dynamics of gravity currents in a channel. *J. Fluid Mech.* **269**, 169–198.

KRÜGER, T., KUSUMAATMAJA, H., KUZMIN, A., SHARDT, O., SILVA, G. & VIGGEN, E.M. 2017 *The Lattice Boltzmann Method*, vol. 10, pp. 4–15. Springer International Publishing.

LOUGHLIN, S.C., CALDER, E.S., CLARKE, A., COLE, P.D., LUCKETT, R., MANGAN, M.T., PYLE, D.M., SPARKS, R.S.J., VOIGHT, B. & WATTS, R.B. 2002 Pyroclastic flows and surges generated by the 25 June 1997 dome collapse, Soufrière Hills Volcano, Montserra. *Geol. Soc. London Memoirs* **21** (1), 191–209.

MARSHALL, C.R., DORRELL, R.M., DUTTA, S., KEEVIL, G.M., PEAKALL, J. & TOBIAS, S.M. 2021 The effect of schmidt number on gravity current flows: the formation of large-scale three-dimensional structures. *Phys. Fluids* **33** (10), 106601.

MEIBURG, E. & KNELLER, B. 2010 Turbidity currents and their deposits. *Annu. Rev. Fluid Mech.* **42** (1), 135–156.

MEIBURG, E., RADHAKRISHNAN, S. & NASR-AZADANI, M.M. 2015 Modeling gravity and turbidity currents: computational approaches and challenges. *Appl. Mech. Rev.* **67** (4), 040802.

MULDER, T. & ALEXANDER, J. 2001 The physical character of subaqueous sedimentary density flows and their deposits. *Sedimentology* **48** (2), 269–299.

OTTOLENGHI, L., ADDUCE, C., INGHILESI, R., ARMENIO, V. & ROMAN, F. 2016 Entrainment and mixing in unsteady gravity currents. *J. Hydraul. Res.* **54** (5), 541–557.

OTTOLENGHI, L., PRESTININZI, P., MONTESSORI, A., ADDUCE, C. & LA ROCCA, M. 2018 Lattice boltzmann simulations of gravity currents. *Eur. J. Mechan.-B/Fluids* **67**, 125–136.

PEAKALL, J. & SUMNER, E.J. 2015 Submarine channel flow processes and deposits: a process–product perspective. *Geomorphology* **244**, 95–120.

REECE, J.K., DORRELL, R.M. & STRAUB, K.M. 2024 Circulation of hydraulically ponded turbidity currents and the filling of continental slope minibasins. *Nat. Commun.* **15** (1), 2075.

ROTTMAN, J.W. & SIMPSON, J.E. 1983 Gravity currents produced by instantaneous releases of a heavy fluid in a rectangular channel. *J. Fluid Mech.* **135**, 95–110.

STOKER, J.J. 2011 *Water Waves: The Mathematical Theory with Applications*. John Wiley & Sons.

TRITTON, D.J. 2012 *Physical Fluid Dynamics*. Springer Science & Business Media.

UNGARISH, M. 2009 *An Introduction to Gravity Currents and Intrusions*. Chapman and Hall/CRC.

UNGARISH, M. & ZEMACH, T. 2005 On the slumping of high Reynolds number gravity currents in two-dimensional and axisymmetric configurations. *Eur. J. Mechan.-B/Fluids* **24** (1), 71–90.

WELLS, M.G. & DORRELL, R.M. 2021 Turbulence processes within turbidity currents. *Annu. Rev. Fluid Mech.* **53**, 59–83.

WILSON, COLIN J.N. 2008 Supereruptions and supervolcanoes: processes and products. *Elements* **4** (1), 29–34.

YANG, X., MEHMANI, Y., PERKINS, W.A., PASQUALI, A., SCHÖNHERR, M., KIM, K., PEREGO, M., PARKS, M.L., TRASK, N. & BALHOFF, M.T. 2016 Intercomparison of 3d pore-scale flow and solute transport simulation methods. *Adv. Water Resour.* **95**, 176–189.

ZHU, R., HE, Z. & MEIBURG, E. 2023 Mixing, entrainment and energetics of gravity currents released from two-layer stratified locks. *J. Fluid Mech.* **960**, A1.